NeuroImage 286 (2024) 120506

Contents lists available at ScienceDirect

NeuroImage

journal homepage: www.elsevier.com/locate/ynimg

Model-based super-resolution reconstruction for pseudo-continuous Arterial Spin Labeling

Quinten Beirinckx [a,d], Piet Bladt [a,d], Merlijn C.E. van der Plas [b], Matthias J.P. van Osch [b], Ben Jeurissen [a,c,d], Arnold J. den Dekker [a,d], Jan Sijbers [a,d,*]

[a] imec-Vision Lab, Department of Physics, University of Antwerp, Antwerp, Belgium
[b] C.J. Gorter MRI Center, Department of Radiology, Leiden University Medical Center, Leiden, The Netherlands
[c] Lab for Equilibrium Investigations and Aerospace, Department of Physics, University of Antwerp, Antwerp, Belgium
[d] μNEURO Research Centre of Excellence, University of Antwerp, Antwerp, Belgium

ARTICLE INFO

Keywords:
Arterial spin labeling
Perfusion
CBF mapping
Super-resolution
Quantitative MRI
Model-based reconstruction

ABSTRACT

Arterial spin labeling (ASL) is a promising, non-invasive perfusion magnetic resonance imaging technique for quantifying cerebral blood flow (CBF). Unfortunately, ASL suffers from an inherently low signal-to-noise ratio (SNR) and spatial resolution, undermining its potential. Increasing spatial resolution without significantly sacrificing SNR or scan time represents a critical challenge towards routine clinical use. In this work, we propose a model-based super-resolution reconstruction (SRR) method with joint motion estimation that breaks the traditional SNR/resolution/scan-time trade-off. From a set of differently oriented 2D multi-slice pseudo-continuous ASL images with a low through-plane resolution, 3D-isotropic, high resolution, quantitative CBF maps are estimated using a Bayesian approach. Experiments on both synthetic whole brain phantom data, and on *in vivo* brain data, show that the proposed SRR Bayesian estimation framework outperforms state-of-the-art ASL quantification.

1. Introduction

Arterial spin labeling (ASL) is a magnetic resonance (MR) imaging technique to noninvasively measure cerebral blood flow (CBF), which is a biomarker for various brain disorders (Alsop et al., 2015; van Osch et al., 2018). ASL uses magnetically labeled arterial blood as an endogenous tracer, where the labeling is performed by inverting the inflowing blood magnetization in a plane proximal to the brain. After a specific period of time, called the post-labeling delay (PLD) time, during which labeled blood travels through the arterial vascular tree towards the brain tissue, a so-called label image is acquired. Additionally, a control image is acquired without prior labeling. The difference between the label and control image yields a perfusion weighted image that isolates the ASL signal. Next, a CBF map is computed from the perfusion weighted image using a perfusion model and a separately acquired calibration image (Alsop et al., 2015).

The consensus paper by Alsop et al. recommends pseudo-continuous ASL (pCASL), background suppression (BS), and segmented 3D readout for clinical implementation of ASL (Alsop et al., 2015). Segmented 3D acquisition schemes use a single excitation per TR, which is optimal for BS (Ye et al., 2000; Krüger and Glover, 2001; Garcia et al., 2005; Maleki et al., 2012; Paschoal et al., 2021). However, 3D readout sequences employ long echo trains, resulting in through-plane blurring due to T_2 decay along the echo train. Splitting the readout into more segments can reduce this blurring, but at the cost of a longer acquisition time and increased sensitivity to inter-shot motion and physiological fluctuations (Hernandez-Garcia et al., 2022). In addition, the long readout time of a 3D imaging sequence holds an increased risk of motion artifacts (Alsop et al., 2015).

As a viable alternative to 3D readout, single-shot 2D multi-slice (MS) readout methods based on echo-planar imaging (EPI) have been suggested (Alsop et al., 2015). 2D readout methods have several advantages over 3D readout methods. First, they have a much shorter readout and are hence less susceptible to motion during readout (Vidorreta et al., 2013, 2014; Alsop et al., 2015). Second, they are less susceptible to spatial blurring due to T_2 decay (Vidorreta et al., 2013). Finally, 2D readout methods are readily available on all systems (Alsop et al., 2015).

However, 2D readout approaches also come with disadvantages. First, 2D MS imaging causes the PLD time to increase in subsequently acquired slices, which results in a significant degradation of the signal-to-noise ratio (SNR) in the last acquired slices due to longitudinal

* Correspondence to: imec-Vision Lab, University of Antwerp, Universiteitsplein 1, B-2610 Antwerpen, Belgium.
E-mail address: jan.sijbers@uantwerpen.be (J. Sijbers).

https://doi.org/10.1016/j.neuroimage.2024.120506
Received 30 October 2023; Received in revised form 28 December 2023; Accepted 2 January 2024
Available online 5 January 2024

relaxation (van Osch et al., 2018). At the same time, however, the slice-wise increase of PLD can help accommodate unbiased CBF estimation in subjects with arterial transit time (ATT) values that increase from inferior to superior slices, which can be considered a consistent finding in most subjects. Second, the use of a separate excitation pulse for every slice complicates BS. In practice, BS can be optimal for only one slice and will be progressively less efficient for other slices (Alsop et al., 2015).

In this work, which is based on a preliminary study (Bladt et al., 2020), we propose an alternative 2D MS based image acquisition and parameter estimation method for single-PLD pCASL that alleviates the main disadvantages of traditional 2D MS imaging, while preserving its advantages. The method relies on MS super-resolution reconstruction (SRR). In this approach, a 3D isotropic high resolution (HR) image or parameter map is estimated from multiple, differently oriented, 2D MS images with a low through-plane resolution. SRR has been shown to improve the inherent trade-off between spatial resolution, SNR, and acquisition time in MRI (Van Reeth et al., 2012; Plenge et al., 2012) and has previously been applied successfully in anatomical imaging (Poot et al., 2010; Van Dyck et al., 2020), diffusion MRI (Poot et al., 2013; Fogtmann et al., 2014; Van Steenkiste et al., 2016), and relaxometry (Van Steenkiste et al., 2017; Bano et al., 2020; Beirinckx et al., 2020, 2022). The current paper introduces SRR in the field of ASL, proposing a model-based MS-SRR framework with joint motion estimation for direct whole brain CBF mapping from 2D MS single-PLD pCASL data. By choosing an SRR acquisition scheme in which low resolution (LR) label-control image pairs are acquired with varying slice-encoding directions, the negative effects of fading BS and increasing PLD values in subsequently acquired slices of the traditional 2D MS readout scheme for pCASL are made independent of location, i.e. averaged out. To explore its potential in ASL, our newly proposed method is evaluated on synthetic whole brain perfusion data. Moreover, our pCASL MS-SRR method is combined with multiband (MB) imaging, also known as simultaneous multi-slice (SMS) imaging, to accelerate image acquisition and hence provide a more constant and thus on average better BS as well as a more constant PLD across slices (van Osch et al., 2018). Finally, our method is validated on *in vivo* brain data, and compared to a conventional single-PLD pCASL experiment with 2D MS readout using a widely used Bayesian inference model (BASIL Chappell et al., 2009; Groves et al., 2009) for CBF quantification.

2. Theory

In what follows, the components of the proposed ASL SRR framework are discussed, namely the SRR forward model (Section 2.1), the single-PLD pCASL signal model, which encapsulates the CBF quantification formula (Section 2.2), and the joint Bayesian estimation framework, for direct CBF mapping with joint motion estimation from LR single-PLD pCASL data (Section 2.3).

2.1. Super-resolution reconstruction forward model

Let $\boldsymbol{s} = \{\boldsymbol{s}_n\}_{n=1}^{2N}$ be the set of N vectorized, noiseless, anisotropic LR 2D MS control (odd n) and N label (even n) magnitude images. Each image $\boldsymbol{s}_n = \{s_{nl}\}_{l=1}^{N_s} \in \mathbb{R}^{N_s \times 1}$ is sampled at the LR grid points $\boldsymbol{y}_n = \{\boldsymbol{y}_{nl}\}_{l=1}^{N_s} \in \mathbb{R}^{3 \times N_s}$ with N_s the number of voxels per LR image, and can be modeled as:

$$\boldsymbol{s}_n = \boldsymbol{D}\boldsymbol{B}\boldsymbol{G}_n\boldsymbol{M}_{\boldsymbol{\theta}_n}\boldsymbol{r}_n \tag{1}$$

where $\boldsymbol{r}_n = \{r_{nj}\}_{j=1}^{N_r} \in \mathbb{R}^{N_r \times 1}$ represents the unknown, noiseless HR image with the same perfusion-weighting as $\boldsymbol{s}_n$ and defined at the targeted isotropic HR grid points $\boldsymbol{x} = \{\boldsymbol{x}_j\}_{j=1}^{N_r} \in \mathbb{R}^{3 \times N_r}$, with N_r the number of voxels of the HR image. Furthermore, $\boldsymbol{M}_{\boldsymbol{\theta}_n} \in \mathbb{R}^{N_r \times N_r}$, $\boldsymbol{G}_n \in \mathbb{R}^{N_r \times N_r}$, $\boldsymbol{B} \in \mathbb{R}^{N_r \times N_r}$, and $\boldsymbol{D} \in \mathbb{R}^{N_s \times N_r}$ are linear operators that describe unintended motion, a known geometric transformation that models the image acquisition with specific slice orientation, spatially invariant blurring, and down-sampling, respectively. The motion operator $\boldsymbol{M}_{\boldsymbol{\theta}_n}$ is modeled as a parametric function of $\boldsymbol{\theta}_n$. Assuming rigid inter-image motion, the parameter vector $\boldsymbol{\theta}_n \in \mathbb{R}^{6 \times 1}$ is given by $\boldsymbol{\theta}_n = \left[t_{xn}, t_{yn}, t_{zn}, \alpha_n, \beta_n, \gamma_n\right]^T$, with t_{xn}, t_{yn}, t_{zn} the translation parameters and α_n, β_n, γ_n the Euler angles that describe rotation around the x, y, and z axis, respectively.

2.2. Single-PLD pCASL signal model

Let $\Delta\boldsymbol{r}_n = \{\Delta r_{nj}\}_{j=1}^{N_r} \in \mathbb{R}^{N_r \times 1}$, with n even, be the difference image $\boldsymbol{r}_{n-1} - \boldsymbol{r}_n$ and let $\boldsymbol{\vartheta}_{\mathrm{rCBF}} = \{\vartheta_{\mathrm{rCBF},j}\}_{j=1}^{N_r} \in \mathbb{R}^{N_r \times 1}$ represent the HR *relative* CBF parameter map to be estimated, expressed in arbitrary units (a.u.). According to the recommended quantification formula for single-PLD pCASL data (Alsop et al., 2015), Δr_{nj} is given by:

$$\Delta r_{nj}(\vartheta_{\mathrm{rCBF},j}) = \vartheta_{\mathrm{rCBF},j}\delta^{-1}\exp\left(-\frac{\mathrm{PLD}_{nj}}{T_{1b}}\right) \quad , \tag{2}$$

with

$$\delta = 6000 \cdot \frac{\lambda}{2\alpha T_{1b}\left(1 - \exp\left(-\frac{\tau}{T_{1b}}\right)\right)} \tag{3}$$

a scalar constant that encapsulates the labeling efficiency α, the brain–blood partition coefficient λ, the labeling duration τ, and the longitudinal relaxation time of blood T_{1b}, which are all assumed to be known from experiment or fixed at their recommended population averages. In Eq. (2), PLD_{nj} is the PLD time that corresponds with the readout time of the corresponding slice within the label image $\boldsymbol{s}_n$ that contains the HR grid point $\boldsymbol{x}_j$. Indeed, each slice of $\boldsymbol{s}_n$ is characterized by a unique PLD that depends on the slice acquisition order. If the MS acquisition proceeds in ascending slice order with a slice readout time t_{read}, the effective PLD in the Mth slice is given by: $(M-1)\times t_{\mathrm{read}} + \mathrm{PLD}_{\mathrm{base}}$, with $\mathrm{PLD}_{\mathrm{base}}$ the time between the end of the labeling pulse train and the readout. In contrast to a conventional pCASL MS acquisition scheme, in a rotated SRR acquisition scheme, PLD_{nj} will depend on the slice direction (Fig. 1(d)). The mathematical model that describes the slice-dependent PLD_{nj} is provided in Appendix A. Note that due to the PLD variations, the virtual HR label images (i.e., $\boldsymbol{r}_n$ with n is even) differ from each other, whereas the virtual HR control images (i.e., $\boldsymbol{r}_n$ with n is odd) are all equal when ignoring BS. Consequently, it follows that the jth voxel of $\boldsymbol{r}_n$ can be modeled as:

$$r_{nj} = \begin{cases} r_{1,j}, & \text{if } n \text{ is odd} \\ r_{1,j} - \Delta r_{nj}(\vartheta_{\mathrm{rCBF},j}), & \text{if } n \text{ is even} \end{cases} . \tag{4}$$

Eq. (4) can be extended to include the effect of BS in 2D MS readout:

$$r_{nj} = \begin{cases} r_{1,j}\, b_{nj}, & \text{if } n \text{ is odd} \\ r_{1,j}\, b_{nj} - \Delta r_{nj}(\vartheta_{\mathrm{rCBF},j}), & \text{if } n \text{ is even,} \end{cases} \tag{5}$$

where $\boldsymbol{b}_n = \{b_{nj}\}_{j=1}^{N_r} \in \mathbb{R}^{N_r \times 1}$ models inversion-recovery nulling for BS, under the assumption that BS is perfect for the first acquired slice and with T_{1t} the T_1 relaxation time of tissue t, i.e. $b_{nj} = 1 - 2 \cdot \exp\left(-\mathrm{TI}_{nj}/T_{1t,j}\right)$, with TI_{nj} the optimal inversion time for perfect BS of the first slice. More details on how to model TI_{nj} for SRR are provided in Appendix B.

Following the recommendations of the ASL white paper (Alsop et al., 2015), a calibration step is needed to translate CBF values in arbitrary units to absolute units of mL/100 g/min of tissue, by voxel-wise dividing the relative CBF map $\boldsymbol{\vartheta}_{\mathrm{rCBF}}$ by a HR proton density weighted calibration image $\boldsymbol{\rho}_{\mathrm{reg}} = \{\rho_{\mathrm{reg},j}\}_{j=1}^{N_r} \in \mathbb{R}^{N_r \times 1}$, registered to the HR reconstruction grid. In this work, we assume $\boldsymbol{\rho}_{\mathrm{reg}}$ to be a known image, acquired from a separate acquisition. This calibration image is essentially a control image without background suppression acquired with the same readout as the ASL data (Clement et al., 2022). As such, the HR CBF parameter map is defined as $\boldsymbol{\vartheta}_{\mathrm{CBF}} = \{\vartheta_{\mathrm{CBF},j}\}_{j=1}^{N_r} =$

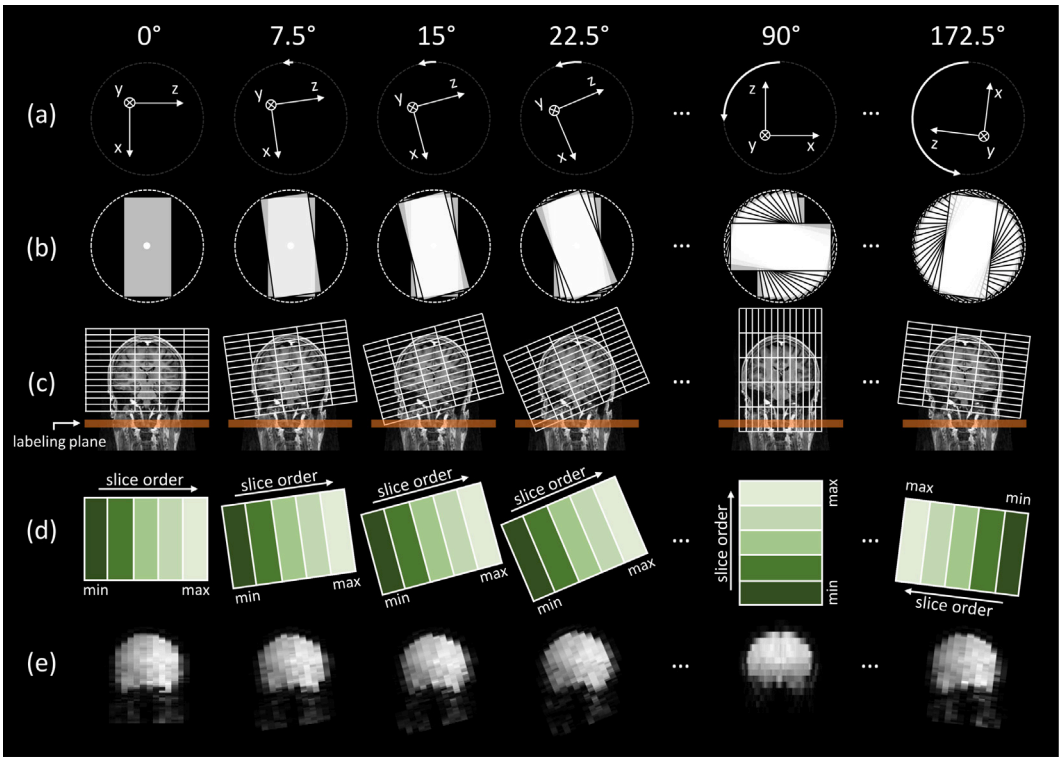

Fig. 1. MS SRR acquisition scheme: (a) acquisition coordinate system; (b) k-space coverage; (c) grid in image space; (d) slice dependent PLDs; (e) coronal LR MS images. The x-, y-, and z-direction represent the frequency-, phase-, and slice-encoding direction, respectively.

$\{\vartheta_{\mathrm{rCBF},j}/\rho_{\mathrm{reg},j}\}_{j=1}^{N_r} \in \mathbb{R}^{N_r\times 1}$. Note that by replacing $\boldsymbol{\vartheta}_{\mathrm{rCBF}}$ with $\boldsymbol{\vartheta}_{\mathrm{CBF}}$ in Eq. (4), a calibrated version of the single-PLD pCASL model for $\boldsymbol{r}_n$ can be obtained.

2.3. Joint Bayesian estimation framework

2.3.1. Maximum a posteriori estimator

Let $\tilde{\boldsymbol{s}} = \{\tilde{\boldsymbol{s}}_n\}_{n=1}^{2N} \in \mathbb{R}^{N_s\times 2N}$ denote the set of $2N$ measured, noisy LR MS images with $\tilde{\boldsymbol{s}}_n = \{\tilde{s}_{nl}\}_{l=1}^{N_s} \in \mathbb{R}^{N_s\times 1}$. Furthermore, let $\boldsymbol{\vartheta} = [\boldsymbol{r}_1^T\ \boldsymbol{\vartheta}_{\mathrm{rCBF}}^T]^T \in \mathbb{R}^{2N_r\times 1}$ and $\boldsymbol{\theta} = \{\boldsymbol{\theta}_n\}_{n=1}^{2N} \in \mathbb{R}^{6\times 2N}$ represent the perfusion parameters and the motion parameters to be estimated, respectively. Following a Bayesian approach, the data $\tilde{\boldsymbol{s}}$ and the parameters $\{\boldsymbol{\vartheta},\boldsymbol{\theta}\}$ are modeled as random variables, where Bayes' theorem gives an expression for the *posterior* distribution of the parameters given the data:

$$p(\boldsymbol{\vartheta},\boldsymbol{\theta}|\tilde{\boldsymbol{s}}) = \frac{p(\tilde{\boldsymbol{s}}|\boldsymbol{\vartheta},\boldsymbol{\theta})p(\boldsymbol{\vartheta})p(\boldsymbol{\theta})}{p(\tilde{\boldsymbol{s}})} \quad , \tag{6}$$

with $p(\tilde{\boldsymbol{s}}|\boldsymbol{\vartheta},\boldsymbol{\theta})$ the conditional probability distribution of $\tilde{\boldsymbol{s}}$ given the parameters $\{\boldsymbol{\vartheta},\boldsymbol{\theta}\}$, $p(\boldsymbol{\vartheta})$ and $p(\boldsymbol{\theta})$ the *prior* distributions that encapsulate the prior knowledge about $\boldsymbol{\vartheta}$ and $\boldsymbol{\theta}$, respectively, and with $p(\tilde{\boldsymbol{s}})$ a normalization factor. When $p(\tilde{\boldsymbol{s}}|\boldsymbol{\vartheta},\boldsymbol{\theta})$ is viewed as a function of the unknown parameters $\{\boldsymbol{\vartheta},\boldsymbol{\theta}\}$ given the data $\tilde{\boldsymbol{s}}$, it is called the *likelihood* function.

For a single-coil acquisition, the noisy voxel intensities $\tilde{s}_{nl}$ can be modeled as Rician distributed random variables, while for a multi-coil acquisition, $\tilde{s}_{nl}$ are governed by a non-central chi distribution (den Dekker and Sijbers, 2014). When the SNR is high enough (>3), which is typically the case for the low resolution voxels $\tilde{s}_{nl}$, both distributions can be well approximated by a Gaussian distribution. If the voxel intensities are additionally assumed to be statistically independent and the standard deviation of the noise σ to be temporally and spatially invariant, the likelihood function $p(\tilde{\boldsymbol{s}}|\boldsymbol{\vartheta},\boldsymbol{\theta})$ can be expressed as:

$$p(\tilde{\boldsymbol{s}}|\boldsymbol{\vartheta},\boldsymbol{\theta}) \propto \exp\left(-\frac{1}{2\sigma^2}\sum_{n=1}^{2N}\sum_{l=1}^{N_s}\left(\tilde{s}_{nl} - s_{nl}(\boldsymbol{\vartheta},\boldsymbol{\theta}_n)\right)^2\right). \tag{7}$$

Furthermore, the prior distributions of the HR parameter maps $\boldsymbol{r}_1$ and $\boldsymbol{\vartheta}_{\mathrm{rCBF}}$, which are assumed to be smooth, are chosen as:

$$p(\boldsymbol{r}_1) \propto \exp\left(-\frac{\lambda_{\boldsymbol{r}_1}}{2}\|\Delta(\boldsymbol{r}_1)\|_2^2\right) \quad \text{and}$$
$$p(\boldsymbol{\vartheta}_{\mathrm{rCBF}}) \propto \exp\left(-\frac{\lambda_{\boldsymbol{\vartheta}_{\mathrm{rCBF}}}}{2}\|\Delta(\boldsymbol{\vartheta}_{\mathrm{rCBF}})\|_2^2\right) \quad , \tag{8}$$

respectively, where $\Delta(\cdot)$ denotes the 3D discrete Laplace operator (Poot et al., 2013), and $\lambda_{\boldsymbol{r}_1} > 0$ and $\lambda_{\boldsymbol{\vartheta}_{\mathrm{rCBF}}} > 0$ are hyper-parameters that control the regularization strengths. For the motion parameters $\boldsymbol{\theta}$, a non-informative prior $p(\boldsymbol{\theta})$ is adopted, assuming $p(\boldsymbol{\theta})$ to be uniform over the range of values for which the likelihood function is non-negligible. The maximum a posteriori (MAP) estimator then maximizes $p(\boldsymbol{\vartheta},\boldsymbol{\theta}|\tilde{\boldsymbol{s}})$ w.r.t. the parameters $\{\boldsymbol{\vartheta},\boldsymbol{\theta}\}$. Hence, by combining Eqs. (6)–(8), we obtain:

$$\{\hat{\boldsymbol{\vartheta}},\hat{\boldsymbol{\theta}}\} = \arg\max_{\boldsymbol{\vartheta},\boldsymbol{\theta}} p(\boldsymbol{\vartheta},\boldsymbol{\theta}|\tilde{\boldsymbol{s}}) = \arg\min_{\boldsymbol{\vartheta},\boldsymbol{\theta}}\left[-\ln p(\boldsymbol{\vartheta},\boldsymbol{\theta}|\tilde{\boldsymbol{s}})\right] \tag{9}$$

$$= \arg\min_{\boldsymbol{\vartheta},\boldsymbol{\theta}}\left[\sum_{n=1}^{2N}\sum_{l=1}^{N_s}\left(\tilde{s}_{nl} - s_{nl}\left(\boldsymbol{\vartheta},\boldsymbol{\theta}_n\right)\right)^2 + \lambda'_{\boldsymbol{r}_1}\|\Delta(\boldsymbol{r}_1)\|_2^2 + \lambda'_{\boldsymbol{\vartheta}_{\mathrm{rCBF}}}\|\Delta(\boldsymbol{\vartheta}_{\mathrm{rCBF}})\|_2^2\right], \tag{10}$$

with $\lambda'_{\boldsymbol{r}_1} = \sigma^2\lambda_{\boldsymbol{r}_1}$ and $\lambda'_{\boldsymbol{\vartheta}_{\mathrm{rCBF}}} = \sigma^2\lambda_{\boldsymbol{\vartheta}_{\mathrm{rCBF}}}$ regularization parameters to be selected by the user. Note that σ does not have to be known or estimated in advance.

2.3.2. Optimization

The optimization problem in Eq. (9) is solved using the *alternating minimization* method, also known as the cyclic block-coordinate descent (cBCD) method (Fessler and Kim, 2011; Beck and Tetruashvili, 2013). In this method, the parameters $\{\boldsymbol{\vartheta},\boldsymbol{\theta}\}$ are split into two blocks that contain the perfusion parameters $\boldsymbol{\vartheta}$, and the motion parameters $\boldsymbol{\theta}$, and

the cost function is successively minimized with respect to each block in a cyclic order:

$$\hat{\boldsymbol{\vartheta}}^{(t+1)} = \arg\min_{\boldsymbol{\vartheta}} \left[\sum_{n=1}^{2N} \sum_{l=1}^{N_s} \left(\bar{s}_{nl} - s_{nl}(\boldsymbol{\vartheta}, \hat{\boldsymbol{\theta}}_n^{(t)}) \right)^2 + \lambda'_{\boldsymbol{r}_1} \|\Delta(\boldsymbol{r}_1)\|_2^2 + \lambda'_{\vartheta_{\mathrm{rCBF}}} \|\Delta(\vartheta_{\mathrm{rCBF}})\|_2^2 \right] \quad \text{(P.1)}$$

$$\hat{\boldsymbol{\theta}}^{(t+1)} = \arg\min_{\boldsymbol{\theta}} \sum_{n=1}^{2N} \sum_{l=1}^{N_s} \left(\bar{s}_{nl} - s_{nl}(\hat{\boldsymbol{\vartheta}}^{(t+1)}, \boldsymbol{\theta}_n) \right)^2 \quad \text{(P.2)}$$

with $\hat{\boldsymbol{\vartheta}}^{(0)} = \boldsymbol{\vartheta}_{\mathrm{ini}}$ the initial values of the HR parameter maps $\boldsymbol{\vartheta}$, and with $\hat{\boldsymbol{\theta}}^{(0)} = \boldsymbol{\theta}_{\mathrm{ini}}$ the initial values of the motion parameters $\boldsymbol{\theta}$, respectively. The procedure is terminated when a maximum number of iterations is exceeded, or when a convergence tolerance on the relative difference of the tissue parameter estimates between consecutive iterations, defined as $\mathcal{E}^{(t)} = \|\hat{\boldsymbol{\vartheta}}^{(t)} - \hat{\boldsymbol{\vartheta}}^{(t-1)}\|_2 / \|\hat{\boldsymbol{\vartheta}}^{(t)}\|_2$, is reached.

The alternating optimization routine requires suitable choices of the convergence tolerances and regularization weights, as well as choosing suitable solvers for model parameter optimization problem (P.1), and the motion parameter optimization problem (P.2). To efficiently solve the linear subproblem (P.1), the Conjugate Gradient Least Squares (CGLS) algorithm was used, in which parameter maps were initialized with zeros. The inter-image motion estimation problem (P.2), on the other hand, is nonlinear and adopts a particularly simple structure when the signal model parameters remain fixed. If the elements of $\boldsymbol{\theta}$ are independent, problem (P.2) can be decoupled into $2N$ optimization problems that can be solved efficiently by parallel operations. Each of these decoupled problems is minimized using a trust-region Newton algorithm (Coleman and Li, 1994), with analytical expressions for the Jacobian to speed up convergence.

2.3.3. Implementation

The proposed method was written in MATLAB and partially in C++. The computational complexity of the proposed algorithm is primarily defined by the Fast Fourier Transform (FFT)-based image warping operators $\boldsymbol{M}_{\theta_n}$ and $\boldsymbol{G}_n$ in Eq. (1) (Beirinckx et al., 2022). To speed up reconstruction, the FFTs of these image warping operators were executed on the GPU. Furthermore, while the forward model given by Eq. (1) treats $\boldsymbol{M}_{\theta_n}$ and $\boldsymbol{G}_n$ as separate operators, in our implementation we combined both operators to limit the number of FFTs and to maximize computational efficiency. Linear operators $\boldsymbol{D}$ and $\boldsymbol{B}$ followed the implementation of Beirinckx et al. (2022). MATLAB parallel computing tools were used to estimate $\boldsymbol{\theta}_n$ for each value of n separately when solving problem (P.2) of the alternating minimization method. A single reconstruction took approximately 19 min for a simulated LR single-PLD pCASL dataset (without motion optimization), and 1 h 10 min for the *in vivo* LR single-PLD pCASL dataset, respectively.

3. Methods

The proposed method, denoted as **SRR-pCASL**, was evaluated in simulation and *in-vivo* experiments, where its performance was compared to that of the following reference methods:

C-pCASL Conventional acquisition of single-PLD pCASL data with 2D MS readout in which each control-label image pair is acquired multiple times at a 3D isotropic high resolution, with an inferior–superior slice-encoding direction, and with an ascending slice readout order. The reconstruction and direct CBF mapping are performed using the *same* joint Bayesian estimation framework as for SRR-pCASL.

BASIL Conventional acquisition of single-PLD pCASL data with 2D MS readout, similar as for C-pCASL. From these data, CBF was quantified using the Bayesian Inference for Arterial Spin Labeling (BASIL) method (Chappell et al., 2009; Groves et al., 2009), which is part of the FSL toolbox (Smith et al., 2004; Woolrich et al., 2009). Default settings were used to process single-PLD data, as described by the BASIL documentation guide and following the recommendations of the consensus paper (Alsop et al., 2015). BASIL uses FSL's *mcflirt* (Jenkinson et al., 2002) to correct for motion between the ASL data and the calibration image. Note that this second reference method is primarily included to verify C-pCASL as a benchmark for optimal traditional CBF quantification w.r.t. SRR-pCASL. As such, a true one-to-one benchmarking between BASIL and the proposed MAP estimation framework is not the main objective, especially since the use of different prior information and motion correction strategies in both approaches complicates a fair comparison.

In addition to the above methods a multiband (MB) imaging version to **SRR-pCASL**, **C-pCASL** and **BASIL** was evaluated to partially prevent longitudinal relaxation effects due to increasing PLD values for ascending slices during acquisition. The corresponding MB augmented methods are denoted as **SRR-pCASL-MB**, **C-pCASL-MB**, and **BASIL-MB**, respectively.

3.1. Simulation experiments

Simulation experiments were set up to evaluate the proposed SRR method for single-PLD pCASL and compare its performance with that of the reference methods. First, to exclude a possible bias in the CBF estimation introduced by misregistration when comparing the different methods, a Monte Carlo simulation experiment was performed where the motion parameters $\boldsymbol{\theta}_n$ were set to $\mathbf{0}$ and no motion correction was performed. Second, a Monte Carlo simulation experiment was performed in which the synthetic pCASL data were corrupted with unwanted inter-image motion to evaluate the estimation of both CBF and motion parameters. To guarantee realistic head movement, the inter-image motion parameters $\{\boldsymbol{\theta}_n\}_{n=1}^{2N}$ were chosen equal to an estimated set of motion parameters obtained using a rigid registration routine on the *in vivo* LR SRR data. A detailed description of this registration routine and the obtained true reference motion parameters for each of the $2N$ pCASL images in the simulation study is provided in section S1.2 of the supplementary file.

3.1.1. Synthetic data generation

Both for the simulations without and with motion, four different synthetic datasets were generated, all having the same underlying HR ground truth parameter maps for CBF, PD and the relaxation time T_{1t} of tissue. These ground-truth parameter maps were generated starting from a 216 × 180 × 180 HR brain phantom with labeled tissue classes supplied by MRiLab (Liu et al., 2017) with a 1 mm^3 isotropic resolution. Gray (GM) and white matter (WM) CBF values of 65 mL/100 g/min and 20 mL/100 g/min, respectively, reported for the healthy human brain, were assigned to the CBF map (Parkes et al., 2004; Zhang et al., 2014; Fan et al., 2016). To assess the identification of hyperintensities (Maier et al., 2021), we additionally simulated a hyperperfusion lesion of 113.75 mL/100 g/min in GM and 50 mL/100 g/min in WM, having a volume equal to 408 mm^3 and 330 mm^3, respectively. Subsequently, the CBF, PD, and T_{1t} maps were resampled onto a 72 × 60 × 60 grid using cubic interpolation with a scale-variant kernel to prevent aliasing, matching a 3D isotropic resolution of 3 mm typical for HR ASL data. Finally, each HR ground-truth parameter map was zero padded to a 80 × 80 × 64 grid, such that it corresponds to the dimensions of the reconstruction grid of the real data experiment (Section 3.2). Starting from these ground truth parameter maps, the following noiseless datasets were generated:

Table 1
Acquisition settings for the synthetic data sets using 2D MS readout. A slice orientation angle of 0° corresponds with the slice-encoding axis directed from left to right, and with the phase-encoding axis perpendicularly directed from anterior to posterior. Each angle listed below is a rotation of the slice-encoding axis around the phase-encoding direction counterclockwise. Therefore, a 90° angle is consistent with an ascending slice order. These rotations are consistent with the rotations visualized in Fig. 1.

	Dataset 1 LR 2D MS	Dataset 2 HR 2D MS	Dataset 3 LR 2D MS MB	Dataset 4 HR 2D MS MB
Slices per slab N_{slice} (#)	16	40	16	40
Acquisition matrix	80 × 80	80 × 80	80 × 80	80 × 80
FOV [mm^3]	240 × 240 × 192	240 × 240 × 120	240 × 240 × 192	240 × 240 × 120
Voxel size [mm^3]	3 × 3 × 12	3 × 3 × 3	3 × 3 × 12	3 × 3 × 3
Labeling duration τ [ms]	1800	1800	1800	1800
PLD_{base} [ms]	1800	1800	1800	1800
PLD range[a] [ms]	1800–2550	1800–3750	1800–2150	1800–2750
Slice readout time t_{read} [ms]	50	60	50	60
Number of control-label pairs N	24	22	24	22
Number of slice encoding directions	24	1	24	1
Slice orientation angles[b] [°]	0, 7.5,…,172.5	90	0, 7.5,…,172.5	90
Multiband factor ω	n.a.	n.a.	2	2
Theoretical scan time[c] T [min:s]	3:30	4:20	3:10	3:30

[a] For a dataset with MB, the PLD range is given for a single band.
[b] For the LR datasets, the slice orientation angles where chosen by rotating the slice stack around the virtual phase encoding axis in increments of $180/N$ degrees. For $N = 24$, each rotational increment is equal to 7.5°.
[c] Defined as $T = 2N \cdot (\tau + \mathrm{PLD}_{base} + N_{slice} \cdot t_{read}/\omega)$.

Dataset 1: LR 2D MS data (for SRR) Whole brain SRR single-PLD pCASL data was simulated assuming the rotational acquisition scheme depicted in Fig. 1. The acquisition settings, shown in Table 1, were chosen equal to those of the *in vivo* SRR experiment described in Section 3.2. $N = 24$ control-label image pairs, each with a unique slice-encoding direction, were simulated by rotating the slice stack around the virtual phase encoding axis, aligned in the anterior–posterior direction, in increments of $180/N$ degrees. The acquisition settings, which include a labeling duration $\tau = 1.8$ s, a time between the end of labeling and the start of readout of the first slice $\mathrm{PLD}_{base} = 1.8$ s, $N_{slice} = 16$ slices with a thickness of 12 mm, an in-plane isotropic resolution of 3 mm, and a readout time per slice $t_{read} = 50$ ms, correspond to a total scan time $T = 2N \cdot (\tau + \mathrm{PLD}_{base} + N_{slice} \cdot t_{read}) \approx 210$ s. The LR control-label image pairs were simulated as follows. Starting from the 3 × 3 × 3 mm^3 HR ground truth CBF, PD, and T_{1t} maps described above, $N = 24$ HR whole-brain control-label image pairs were generated using Eq. (5), each with a unique PLD map. Next, for each HR control-label pair, a 3 × 3 × 12 mm^3 LR version was computed using the SRR forward model (Eq. (1)).

Dataset 2: HR 2D MS data Whole brain single-PLD data was simulated assuming a 2D MS acquisition with an isotropic spatial resolution of 3 × 3 × 3 mm^3. The acquisition settings, which are tabulated in Table 1, were chosen identical to those of the *in vivo* experiment described in Section 3.2, except for the use of MB imaging, which was ignored in this dataset. Assuming $N_{slice} = 40$ slices with a thickness of 3 mm, $\tau = 1.8$ s, $\mathrm{PLD}_{base} = 1.8$ s, and $t_{read} = 60$ ms, $N = 22$ HR control-label image pairs were simulated, leading to a longer total scan time than the *in vivo* experiment (see also dataset 4). Starting from the HR ground truth CBF, PD, and T_{1t} maps, Eq. (5) was used to generate a HR control-label image pair where the PLD increased along the inferior–superior slice-encoding direction, following the recommended ascending slice readout order (Alsop et al., 2015). Subsequently, the HR image pair was blurred by applying a spatially invariant 3D point spread function that corresponds with an MS acquisition at 3D isotropic spatial resolution.

Dataset 3: LR 2D MS MB data (for SRR) To generate dataset 3, the procedure used to generate dataset 1 was repeated assuming MB imaging with an MB factor equal to 2. That is, an MB version of dataset 1 was generated assuming that slice n and slice $n + N_{slice}/2$, with $n = 1, 2, \ldots, N_{slice}/2$, were acquired at the same time, hence with the same PLD. The simultaneous acquisition of two slices with MB would reduce the scan time of dataset 3 compared to dataset 1, although the labeling duration and the PLD would still account for most of the scan time. The main advantage of MB will be a closer to optimal BS over the whole volume.

Table 2
Acquisition settings for SRR data and conventionally acquired data using 2D MS readout. A slice orientation angle of 0° corresponds with the slice-encoding axis directed from left to right, and with the phase-encoding axis perpendicularly directed from anterior to posterior. Each angle listed below is a rotation of the slice-encoding axis around the phase-encoding direction counterclockwise. Therefore, a 90° angle is consistent with an ascending slice order. These rotations are consistent with the rotations visualized in Fig. 1.

	LR data for SRR	Conventional HR data
Slices per slab (#)	16	40
Acquisition matrix	80 × 80	80 × 80
FOV [mm^3]	240 × 240 × 192	240 × 240 × 120
Voxel size [mm^3]	3 × 3 × 12	3 × 3 × 3
TR [ms]	4400	4800
Labeling duration [ms]	1800	1800
PLD_{base} [ms]	1800	1800
PLD range[a] [ms]	1800–2550	1800–2750
Number of control-label pairs	24	22
Number of slice encoding directions	24	1
Slice orientation angles [°]	0, 7.5,…,172.5	90
SMS (multiband factor)	n.a.	yes (factor 2)
Total scan time [min:s]	3:30	3:30

[a] For the conventional HR data, the PLD range is given for a single band.

Dataset 4: HR 2D MS MB data To generate dataset 4, the procedure used to generate dataset 2 was repeated assuming MB imaging with an MB factor equal to 2. As such, the acquisition settings were identical to those of the *in vivo* experiment described in Table 2, resulting in the same total scan time as dataset 1 and the *in vivo* scan to allow a fair comparison.

Finally, noise was added to the generated datasets. To facilitate an extensive Monte Carlo study, for each dataset, $N_{MC} = 100$ noise realizations were generated by adding zero-mean, Gaussian distributed noise with standard deviation $\sigma = \sqrt{\sigma_0^2 + \sigma_P^2}$, with σ_0 the standard deviation of the raw noise component, including thermal and scanner noise, and σ_P the standard deviation of the physiological noise component (Krüger and Glover, 2001). Unlike σ_0, σ_P is proportional to

the signal strength S, i.e., $\sigma_P = cS$, with c a scaling factor. Values for σ_0 and c in each dataset were chosen to match the temporal SNR (tSNR) values observed in the *in vivo* data. To this end, a voxel-wise tSNR map was calculated from the conventional HR 2D EPI data set (Table 2), where the tSNR was defined per voxel as $\mu_{\Delta r_{nj}}/\sigma_{\Delta r_{nj}}$, with $\mu_{\Delta r_{nj}}$ the temporal voxel-wise mean and $\sigma_{\Delta r_{nj}}$ the temporal voxel-wise standard deviation of the difference images $\{\Delta \boldsymbol{r}_n\}_{n=1}^{N}$, obtained from the N single-PLD pCASL label-control repetitions. Furthermore, an overall tSNR value was obtained by calculating the spatial mean inside a brain mask of the voxel-wise tSNR map. This procedure resulted in a tSNR ranging from approximately 0.2, in brain regions with almost no BS, to 3.4, in brain regions with perfect BS. Subsequently, values for σ_0 and c were tuned to match those tSNR values in the simulated datasets. Fig. S1 of the supplementary file shows the voxel-wise tSNR map obtained from the conventional HR *in vivo* data alongside the tSNR maps used in the simulation experiment, as well as a comparison in overall tSNR value. Note that for the LR control-label images of dataset 1 and 3, the tSNR increased approximately 4-fold as a result of the increased slice thickness of those images when using the SRR forward model (Eq. (1)), as signal scales linearly with the imaged volume. The process of simulating (one noise realization of) dataset 1 is summarized in a flowchart in Fig. 2 for the simulations with unwanted inter-image motion, and in Fig. S2 for the simulations without motion.

3.1.2. Parameter estimation

SRR-pCASL and SRR-pCASL-MB were applied to all noise realizations of dataset 1 and 3, respectively, whereas C-pCASL & BASIL and C-pCASL-MB & BASIL-MB were applied to dataset 2 and 4, respectively. For the simulation experiments with motion, the parameter optimization routine used in C-pCASL, C-pCASL-MB, SRR-pCASL, and SRR-pCASL-MB alternated between (P.1) and (P.2). For the outer loop iterations combining both (P.1) and (P.2), a convergence tolerance on the relative difference of the tissue parameters between consecutive iterations $\mathcal{E}^{(t)}$ was set at $\mathcal{E}_{\min} = 10^{-4}$, with a maximum number of 10 iterations. Regarding the inner iterations, the convergence tolerance on the relative difference of the tissue parameters between consecutive iterations for (P.1) was also set at $\mathcal{E}_{\min} = 10^{-4}$, with the maximum number of iterations set at 120. Each of the decoupled sub-problems of (P.2) was solved using a lower bound of $\mu = 10^{-6}$ on the step size as convergence tolerance, i.e. iterations end when $\|\boldsymbol{\theta}^{(t-1)} - \boldsymbol{\theta}^{(t)}\|_2 < \mu$. The regularization parameters in (P.1) were heuristically set to $\lambda'_{\boldsymbol{r}_1} = 1.6\cdot10^{-3}$ and $\lambda'_{\mathrm{rCBF}} = 2.0\cdot10^{-5}$, balancing the trade-off between the data consistency objective and the regularization objectives of the tissue parameter maps $\boldsymbol{r}_1$ and $\vartheta_{\mathrm{rCBF}}$, respectively. To compare the estimation methods independent of the choice of regularization parameters, the same values for $\lambda'_{\boldsymbol{r}_1}$ and λ'_{rCBF} were used for C-pCASL, C-pCASL-MB, SRR-pCASL and SRR-pCASL-MB. For the simulations without motion, only (P.1) was solved in the parameter optimization routine of C-pCASL, C-pCASL-MB, SRR-pCASL, and SRR-pCASL-MB, using the same tolerance settings and regularization parameters for (P.1) as for the simulations with motion. For BASIL and BASIL-MB, motion correction using FSL's *mcflirt* was only turned on in the simulations with motion. To facilitate voxel-wise division with the calibration image $\boldsymbol{\rho}_{\mathrm{reg}}$ in the simulation experiments, the $\boldsymbol{\rho}_{\mathrm{reg}}$ image and the first control image were assumed to be perfectly aligned and the first control image was used as a reference target image when estimating the motion of the other images, both for the proposed framework and for BASIL.

3.1.3. Performance analysis

The CBF estimates obtained by the individual methods were compared based on a voxel-wise analysis of the accuracy and precision of each method using the following performance measures (Beirinckx et al., 2020, 2022):

Absolute relative bias (arBias), which quantifies the *accuracy* of an estimator, calculated as $\left|(\bar{\hat{\vartheta}}_{\mathrm{CBF}} - \vartheta_{\mathrm{CBF}}) \oslash \vartheta_{\mathrm{CBF}}\right|$, where $\bar{\hat{\vartheta}}_{\mathrm{CBF}}$ and ϑ_{CBF} refer to the CBF maps which contain the element-wise sample mean of the N_{MC} estimates $\hat{\vartheta}_{\mathrm{CBF}}$, and the true reference values, respectively, and where $\oslash$ denotes the element-wise division operator.

Relative standard deviation (rSTD), which quantifies the *precision* of an estimator, calculated as $\left(\frac{N_{\mathrm{MC}}}{N_{\mathrm{MC}}-1}\overline{(\hat{\vartheta}_{\mathrm{CBF}} - \bar{\hat{\vartheta}}_{\mathrm{CBF}})\circ(\hat{\vartheta}_{\mathrm{CBF}} - \bar{\hat{\vartheta}}_{\mathrm{CBF}})}\right)^{\circ\frac{1}{2}} \oslash \vartheta_{\mathrm{CBF}}$, where $\circ$ and the superscript $\circ\frac{1}{2}$ denote the Hadamard product and element-wise square-root operator, respectively.

Relative root-mean-squared error (rRMSE), which is a combined measure of accuracy and precision, calculated as $\left(\overline{(\hat{\vartheta}_{\mathrm{CBF}} - \vartheta_{\mathrm{CBF}})\circ(\hat{\vartheta}_{\mathrm{CBF}} - \vartheta_{\mathrm{CBF}})}\right)^{\circ\frac{1}{2}} \oslash \vartheta_{\mathrm{CBF}}$.

In addition, the spatial mean of each of these performance measure maps was computed, yielding $\overline{arBias}$, $\overline{rSTD}$, and $\overline{rRMSE}$, respectively. To further assess image quality of the estimated CBF maps compared to the ground truth HR CBF map, average structural similarity index measure (SSIM) and peak SNR (PSNR) values were obtained for each method by calculating the sample mean of the SSIM and PSNR values obtained for each of the N_{MC} realizations.

To assess the ability of the different frameworks to estimate motion, the following performance measure was used:

Motion component root-(mean)-mean-squared-error (RMMSE), which is defined as $\left(\frac{1}{2N}\sum_{n=1}^{2N}\overline{(\hat{\theta}_n - \theta_n)\circ(\hat{\theta}_n - \theta_n)}\right)^{\circ\frac{1}{2}}$, where θ_n refers to the true reference value and the operator $\overline{(\cdot)}$ denotes the element-wise sample mean over the N_{MC} estimates $\hat{\theta}_n$.

Next, to visually compare the estimated CBF values against the reference CBF values, a 2D scatter plot for each method was generated between $\bar{\hat{\vartheta}}_{\mathrm{CBF}}$ and ϑ_{CBF}. Additionally, following the definition of Delbany et al. (2019), the SNR gain map $\boldsymbol{\Gamma}_{X,Y} \in \mathbb{R}^{N_r\times1}$ between method X and method Y was calculated as $\boldsymbol{\Gamma}_{X,Y} = \mathbf{SNR}_X \oslash \mathbf{SNR}_Y$. Here, $\mathbf{SNR}_X$ represents the average SNR map of the reconstructed CBF maps in the simulation experiments for method X, which was calculated as the ratio of the element-wise sample mean and standard deviation of the N_{MC} estimates $\hat{\vartheta}_{\mathrm{CBF},X}$ for method X, i.e., $\mathbf{SNR}_X = \bar{\hat{\vartheta}}_{\mathrm{CBF},X} \circ \left(\frac{N_{\mathrm{MC}}}{N_{\mathrm{MC}}-1}\overline{(\hat{\vartheta}_{\mathrm{CBF},X} - \bar{\hat{\vartheta}}_{\mathrm{CBF},X})\circ(\hat{\vartheta}_{\mathrm{CBF},X} - \bar{\hat{\vartheta}}_{\mathrm{CBF},X})}\right)^{\circ\left(-\frac{1}{2}\right)}$. Note that $\boldsymbol{\Gamma}_{X,Y}$ incorporates both the SNR gain due to the use of a different acquisition strategy as well as due to a different reconstruction algorithm being used between both methods. Finally, the spatial mean of each SNR gain map was computed, yielding overall SNR gain values $\overline{\Gamma}_{X,Y}$ between the different methods.

3.2. Real data experiment

The performance of the proposed SRR-pCASL method was also evaluated using *in vivo* brain MS single-PLD pCASL data from a healthy volunteer (adult, male, 29 years old), acquired using a 32-channel head coil on a 3 Tesla-scanner (Achieva, Philips Healthcare). Ethical approval from the local institutional review board was obtained and an informed consent was signed by the volunteer. The pCASL data was acquired using a single-shot 2D EPI readout method, as recommended by Alsop et al. (2015). LR MS data for SRR as well as conventional MB MS data directly acquired at high resolution were collected using the acquisition settings tabulated in Table 2. Data sets were acquired without slice gap. A larger FOV for the LR data set compared to that of the conventional HR data set is needed because the entire brain

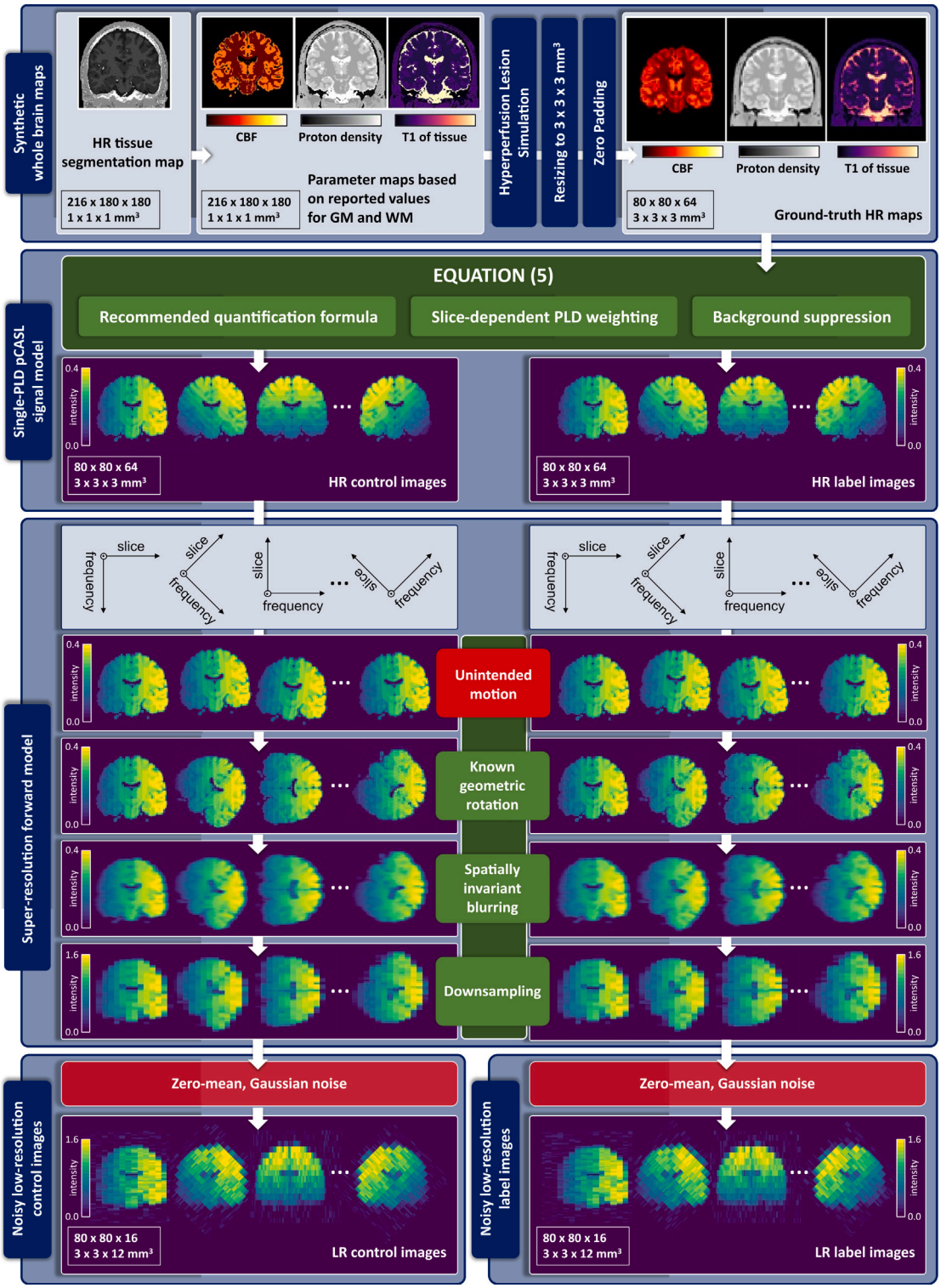

Fig. 2. A flowchart of the data simulation process for single-PLD pCASL data using SRR, in correspondence with the procedure outlined in Section 3.1. Coronal slices are shown for four slice-encoding directions, illustrating the forward modeling of HR ground-truth parameter maps to LR MS images. Signal intensities of the control and label images are shown in arbitrary units.

has to be within the FOV for each rotation angle. Also note that, even though the readout time is significantly longer when acquiring 40 slices instead of 16, this results in only 2 control-label image pairs less for the conventional HR dataset compared to the LR dataset, given a fixed total scan time for both protocols (cfr. Table 2). This is a direct consequence of the fact that the labeling duration and the PLD take up most of the scan time. ASL imaging was performed in combination with background suppression, which consisted of a saturation pulse immediately before labeling and inversion pulses at 1680 and 2830 ms after the saturation pulse. In addition to the pCASL data, a proton density weighted calibration image was acquired without labeling and background suppression at isotropic high resolution for absolute CBF quantification. CBF map estimates were obtained from the LR MS data using the proposed SRR-pCASL method, and compared to the CBF maps

Table 3
Quantitative performance measures with standard error (SE) for the whole brain simulation experiment **without motion**, calculated over $N_{MC} = 100$ reconstruction results for CBF mapping, for each respective readout scheme and reconstruction framework. For each performance measure, the value of the best performing strategy is highlighted in bold.

	BASIL		C-pCASL		SRR-pCASL		BASIL-MB		C-pCASL-MB		SRR-pCASL-MB	
	Value	SE	Value	SE	Value	SE	Value	SE	Value	SE	Value	SE
SSIM	0.9833	1e−4	0.9846	1e−4	0.9927	1e−4	0.9894	1e−4	0.9905	1e−4	**0.9940**	1e−4
PSNR [dB]	30.97	0.02	30.99	0.01	32.33	0.01	32.28	0.03	32.17	0.01	**32.45**	0.01
$\overline{\text{arBias}}$ [%]	7.15	0.02	5.87	0.02	4.59	0.01	5.33	0.02	**4.12**	0.01	4.79	0.02
$\overline{\text{rSTD}}$ [%]	17.15	0.03	17.29	0.03	11.71	0.02	13.87	0.02	13.81	0.02	**10.07**	0.02
$\overline{\text{rRMSE}}$ [%]	19.27	0.04	18.76	0.03	13.07	0.02	15.42	0.02	14.81	0.02	**11.68**	0.02

estimated from the conventional MS MB data using BASIL-MB and C-pCASL-MB. For the acquisition of the conventional HR MS ASL data, an MB factor of 2 was used to limit ASL signal loss in the upper part of the brain. In contrast, MB was not used in the acquisition of the LR SRR-pCASL data because an MB acquisition required a mandatory calibration scan to be performed before the acquisition of each LR image pair with adjusted slice orientation. As a result, the condition of equal total scan time for the conventional HR dataset and the SRR-pCASL dataset would no longer apply.

The parameter optimization routine used in C-pCASL-MB and SRR-pCASL alternated between (P.1) and (P.2). For the outer loop iterations combining both (P.1) and (P.2), a convergence tolerance on the relative difference of the tissue parameters between consecutive iterations $\mathcal{E}^{(t)}$ was set at $\mathcal{E}_{\min} = 10^{-3}$, with a maximum number of 10 iterations. Regarding the inner iterations, the convergence tolerance on the relative difference of the tissue parameters between consecutive iterations for (P.1) was also set at $\mathcal{E}_{\min} = 10^{-3}$, with the maximum number of iterations set at 120. Each of the decoupled sub-problems of (P.2) was solved using a lower bound of $\mu = 10^{-3}$ on the step size as convergence tolerance, i.e. iterations end when $\|\boldsymbol{\theta}^{(t-1)} - \boldsymbol{\theta}^{(t)}\|_2 < \mu$. Regularization weights for the *in vivo* reconstructions were heuristically set at $\lambda'_{r_1} = 8 \cdot 10^{-3}$ and $\lambda'_{\text{rCBF}} = 1 \cdot 10^{-4}$, again similar for C-pCASL-MB and SRR-pCASL. The *in vivo* data for BASIL-MB was motion corrected using FSL's *mcflirt* (Jenkinson et al., 2002).

4. Results

4.1. Simulation experiments

4.1.1. Simulation experiments without motion

Table 3 summarizes the results of the whole brain simulation CBF mapping experiments in terms of the average SSIM, PSNR, $\overline{arBias}$, $\overline{rSTD}$, and $\overline{rRMSE}$, for BASIL, C-pCASL, and SSR-pCASL (with and without MB). For each performance measure, the best performing framework is highlighted in bold. It follows from Table 3 that SRR-pCASL consistently resulted in higher average SSIM and PSNR values compared to traditional CBF quantification with BASIL and C-pCASL. Of all methods studied, SRR-pCASL-MB outperformed the other approaches in terms of average SSIM and PSNR. C-pCASL-MB had the lowest $\overline{arBias}$ value of all methods, and performed best in terms of overall accuracy. SRR-pCASL and SRR-pCASL-MB had the lowest $\overline{rSTD}$ values, outperforming the other methods in terms of overall precision. In terms of overall RMSE, being a measure that incorporates both accuracy and precision, SRR-pCASL outperformed BASIL and C-pCASL, having an $\overline{rRMSE}$ value that is about 30% and 32% smaller than that of C-pCASL and BASIL, respectively. The addition of MB provided consistent improvement for each performance measure for each method, except for SRR-pCASL-MB where the $\overline{arBias}$ value slightly increased. Yet, combining SRR-pCASL with MB, resulting in SRR-pCASL-MB, provided a notable improvement in CBF estimation precision and RMSE. Indeed, $\overline{rSTD}$ and $\overline{rRMSE}$ for SRR-pCASL-MB decreased with about 14% and 10% compared to SRR-pCASL, respectively.

Fig. 3 shows coronal CBF maps estimated with each reconstruction framework as well as their absolute value of the rBias, rSTD, and rRMSE. Different aspects stand out. First, SRR-pCASL outperformed single-orientation pCASL in terms of CBF estimation accuracy, as illustrated by the coronal mid-slice of the arBias. For example, for BASIL a clear bias existed for gray matter estimates in the outer edges of the brain, while for C-pCASL there existed a significant bias in some voxels in the upper part of the brain. The latter may be attributed to the SNR of the ASL signal becoming critically low in these slices, which have the longest effective PLDs and the lowest degree of BS. For SRR-pCASL, the accuracy of the CBF estimation was more uniform across the brain, with no apparent differences between tissue types, or between top or lower parts of the brain. Second, the rSTD of the CBF estimates obtained using BASIL and C-pCASL increased from the lower parts of the brain towards the top parts of the brain (third row of Fig. 3). When using SRR-pCASL, on the other hand, the precision of CBF estimation was much more uniform, per tissue type, throughout the brain (Fig. 3). Furthermore, the addition of MB led to a reduction of the rSTD for each method. Whereas for BASIL-MB and C-pCASL-MB the precision improvement was limited to slices acquired in the second band only, for SRR-pCASL-MB these improvements were obtained across the whole brain. Third, in terms of rRMSE, SRR-pCASL clearly outperformed the other methods without MB, as indicated by the visibly darker rRMSE maps in the fourth row of Fig. 3. Here, the same trends as for the precision maps in Fig. S6 are visible, showing both an increase in the rRMSE for ascending slices during acquisition for BASIL and C-pCASL, and a more uniform rRMSE of the CBF estimation across brain regions for SRR-pCASL.

Fig. 5 (left) shows the locations of the transverse slices that were selected to visualize the variations in CBF estimation on a slice level. Each transverse slice is characterized by a unique PLD and degree of BS, depending on the acquisition settings of the processed dataset for each CBF estimation method. Ground truth values of CBF for these slice locations are given in the leftmost column of Fig. 6, including the GM and WM hyperperfusion lesions denoted by the white arrows in the fourth axial slice. Fig. 6 also shows the rRMSE maps for each slice location and method. Only slices D and E, which were positioned halfway and at the beginning of the second band, respectively, showed a lower rRMSE for BASIL-MB and C-pCASL-MB compared to BASIL and C-pCASL, respectively. Whereas for BASIL-MB and C-pCASL-MB the rRMSE improvement was limited to slices acquired in the second band only, for SRR-pCASL-MB these improvements were obtained across all slices. Axial slice views of the absolute value of the rBias and the rSTD maps, corresponding with the slice locations of Fig. 5, are included in Figs. S5-S6 of the supplementary material. Furthermore, to appreciate resolution enhancements and to ease a qualitative and visual comparison of the CBF map estimated by each method, the supplementary file also includes two additional figures, Fig. S3 and Fig. S4. These figures show orthogonal slice views of the simulated 2D control images for each simulated dataset in comparison with the estimated HR CBF map per framework, and zoomed close-ups of this CBF map in comparison with the ground truth CBF map as a reference, respectively. Additionally, to demonstrate that the potential of SRR is not confined to a particular resolution, a simulation experiment was performed where a $2 \times 2 \times 2$ mm^3 CBF map was super-resolution reconstructed from LR pCASL images with a resolution of $2 \times 2 \times 16$ mm^3. Acquisition settings and results for this additional simulation experiment are summarized in Table S1 and Fig. S7 of the supplementary file.

Next, Fig. 8 shows the average estimated CBF values against the reference CBF values in a 2D scatter plot for BASIL (left), C-pCASL

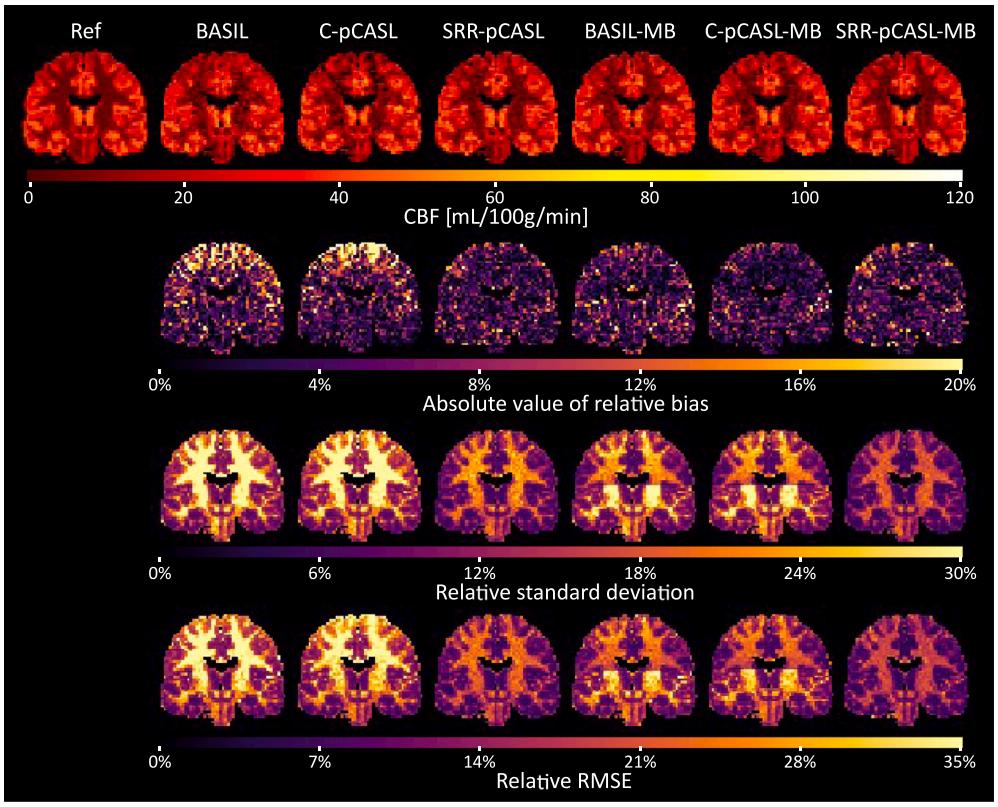

Fig. 3. Coronal mid-slices of the CBF estimates and the corresponding quantitative performance measures for the whole brain simulation experiment **without motion**. The first row shows the numerical ground truth (left), followed by the estimated CBF maps for each method. Next, rows 2–4 show the absolute value of the relative bias, relative standard deviation, and relative RMSE, respectively, computed from the $N_{MC} = 100$ simulations.

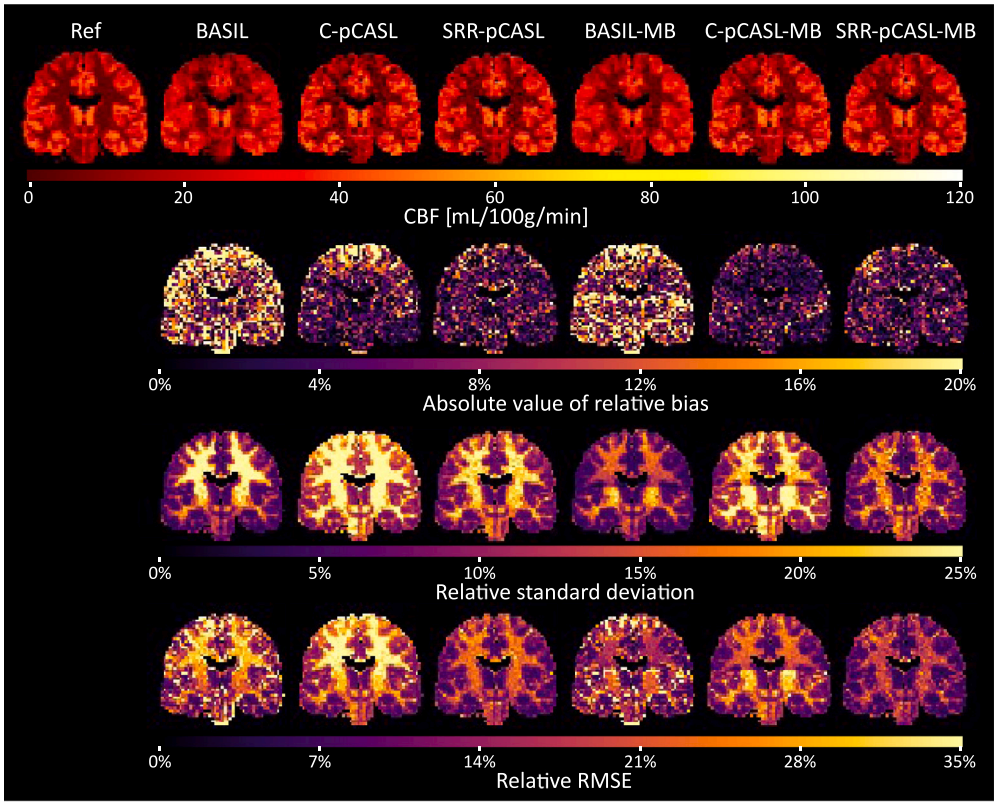

Fig. 4. Coronal mid-slices of the CBF estimates and the corresponding quantitative performance measures for the whole brain simulation experiment **with motion**. The first row shows the numerical ground truth (left), followed by the estimated CBF maps for each method. Next, rows 2–4 show the absolute value of the relative bias, relative standard deviation, and relative RMSE, respectively, computed from the $N_{MC} = 100$ simulations.

Table 4
Quantitative performance measures with standard error (SE) for the whole brain simulation experiment **with motion**, calculated over N_{MC} = 100 reconstruction results for CBF mapping, for each respective readout scheme and reconstruction framework. For each performance measure, the value of the best performing strategy is highlighted in bold.

	BASIL		C-pCASL		SRR-pCASL		BASIL-MB		C-pCASL-MB		SRR-pCASL-MB	
	Value	SE	Value	SE	Value	SE	Value	SE	Value	SE	Value	SE
SSIM	0.9705	1e−4	0.9845	1e−4	0.9920	1e−4	0.9825	1e−4	0.9900	1e−4	**0.9936**	1e−4
PSNR [dB]	28.56	0.02	30.79	0.01	31.54	0.01	30.41	0.03	31.86	0.01	**32.29**	0.01
$\overline{\text{arBias}}$ [%]	15.86	0.05	6.27	0.02	5.51	0.02	12.92	0.04	**4.61**	0.02	5.37	0.02
$\overline{\text{rSTD}}$ [%]	10.41	0.03	17.30	0.03	11.70	0.02	**8.35**	0.02	13.85	0.02	9.87	0.02
$\overline{\text{rRMSE}}$ [%]	20.75	0.05	18.95	0.03	13.54	0.02	16.55	0.04	15.07	0.02	**11.84**	0.02
RMMSE	Value	SE	Value	SE	Value	SE	Value	SE	Value	SE	Value	SE
t_x [mm]	0.2	0.1	**0.0016**	3e−4	0.0020	3e−4	0.3	0.1	0.0021	3e−4	0.0028	4e−4
t_y [mm]	0.11	0.03	0.0034	4e−4	0.017	1e−3	0.18	0.03	**0.0006**	2e−4	0.0094	8e−4
t_z [mm]	0.27	0.06	**0.0015**	2e−4	0.019	1e−3	0.56	0.09	0.0019	3e−4	0.042	2e−3
α [deg]	0.8	0.2	**0.0004**	1e−4	0.0106	9e−4	0.8	0.2	0.0005	2e−4	0.021	1e−3
β [deg]	0.20	0.05	**0.0004**	1e−4	0.0019	4e−4	0.3	0.1	**0.0004**	1e−4	0.0042	6e−4
γ [deg]	0.5	0.2	0.0014	3e−4	0.0022	3e−4	0.8	0.2	**0.0010**	2e−4	0.0043	6e-4

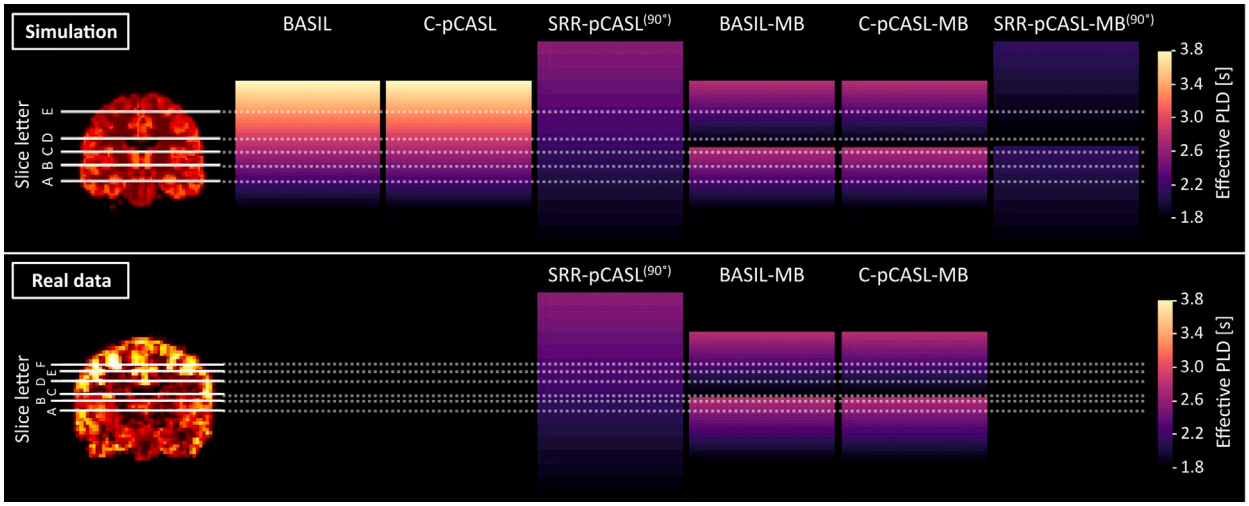

Fig. 5. Top left: locations of the transverse slices for the whole brain simulation experiment (shown in Fig. 6). Bottom left: locations of the transverse slices for the real data experiment (shown in Fig. 11). In addition, coronal mid-slice views of the slice-dependent effective PLD matrix are shown for each approach, reflecting the increase in PLD along the slice-encoding direction, starting from a PLD_{base} value of 1.8 s. Since for SRR-pCASL the effective PLD matrix rotates with the slice orientation of each LR image (see Fig. 1), only the effective PLD matrix corresponding with a slice orientation angle of 90° is shown for SRR-pCASL and SRR-pCASL-MB, consistent with an ascending slice order. Note that missing data in the bottom panel is due to these scans not being acquired in the real data experiment.

(mid), and SRR-pCASL (right) without (top) and with (bottom) MB. As indicated by the narrower distribution (i.e. better precision) and the higher number of voxels that match the ground truth values (i.e. better accuracy), SRR-pCASL and SRR-pCASL-MB outperformed the other methods. Finally, Table 5 summarizes the overall SNR gains between the different methods. SRR-pCASL outperformed the other methods in terms of SNR of the estimated CBF map, as illustrated by the overall SNR gains over BASIL and C-pCASL, even if these methods exploited MB during acquisition. The SNR gain was maximal when SRR-pCASL was combined with MB.

4.1.2. Simulation experiments with motion

Table 4 summarizes the obtained quantitative performance measures for the whole brain simulation CBF mapping experiments with motion. It follows from Table 4 that the need to estimate unwanted motion during the CBF reconstruction degrades the average SSIM, PSNR, $\overline{arBias}$, and $\overline{rRMSE}$ value for each method. This effect is most pronounced for BASIL and BASIL-MB, where motion between the pCASL images was corrected using a registration routine prior to CBF quantification. Without any exception, the addition of MB provided consistent improvement for each performance measure for each method. Similar to the simulations without motion, C-pCASL-MB yielded the lowest $\overline{arBias}$ value of all methods, and performed best in terms of overall accuracy. For BASIL and BASIL-MB, the $\overline{arBias}$ value decreased by more than a factor of 2 compared to the simulations without motion, indicating a considerable drop in accuracy. In terms of overall precision, quantified by the $\overline{rSTD}$ value, C-pCASL and SRR-pCASL performed very similar compared to the simulations without motion (Table 3), whereas BASIL and BASIL-MB showed a noticeable improvement in $\overline{rSTD}$. In terms of overall RMSE, SRR-pCASL clearly outperformed the other approaches without MB, having an $\overline{rRMSE}$ value that is about 34% and 28% smaller than that of BASIL and C-pCASL, respectively. A similar observation is true when MB was added, with SRR-pCASL-MB outperforming the other methods in terms of overall RMSE, having an $\overline{rRMSE}$ value that is about 24% and 21% smaller than that of BASIL-MB and C-pCASL-MB, respectively. For BASIL and BASIL-MB, which apply an adaptive spatial smoothing to the estimated perfusion image, the increased precision (reduced $\overline{rSTD}$) somewhat compensates for the reduced accuracy (increased $\overline{arBias}$), compared to the simulations without motion (Table 3). This compensating effect also follows from Fig. 4, which shows coronal mid-slices of the CBF estimates and the corresponding quantitative performance measures for the simulation experiment with motion. As indicated by the coronal mid-slice of the arBias (second row of Fig. 4), a clear bias could be noted for BASIL and BASIL-MB in all areas of the brain, whereas a reduced precision could be observed from the rSTD map (third row of Fig. 4), most notably for gray matter voxels.

In addition, Table 4 also summarizes the motion component RMMSE for each of the six rigid motion components. The proposed framework

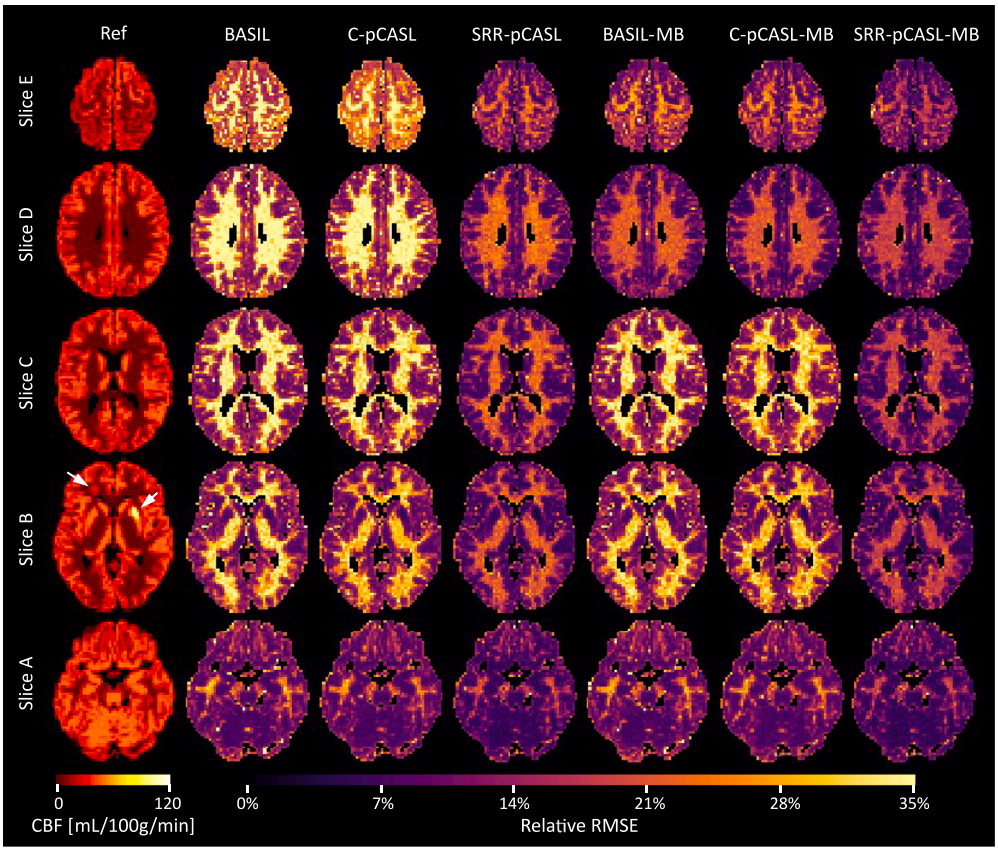

Fig. 6. Relative RMSE maps for CBF, calculated from the reconstruction results of the whole brain simulation experiment **without motion**. For each method, five transverse slices are shown, corresponding with the slice letter convention in Fig. 5. Overall relative RMSE values are summarized in Table 3. The numerical ground truth CBF map is shown in column 1. Both hyperperfusion lesions are indicated by white arrow marks in slice B of this ground truth CBF map.

Table 5
The overall SNR gain ($\overline{\Gamma}_{X,Y}$) with standard error (SE) between reconstruction methods as assessed by the whole brain simulation experiment **without motion**, calculated over the $N_{MC} = 100$ reconstruction results for CBF mapping. Note that row labels refer to method X, while column labels refer to method Y, in line with the definition of $\overline{\Gamma}_{X,Y}$ in Section 3.1.3.

$\overline{\Gamma}_{X,Y}$	BASIL		C-pCASL		SRR-pCASL		BASIL-MB		C-pCASL-MB		SRR-pCASL-MB	
	Value	SE	Value	SE	Value	SE	Value	SE	Value	SE	Value	SE
BASIL	1.000	0.000	1.047	0.001	0.709	0.001	0.845	0.001	0.859	0.001	0.623	0.001
C-pCASL	0.973	0.001	1.000	0.000	0.686	0.001	0.822	0.001	0.831	0.001	0.604	0.001
SRR-pCASL	1.446	0.001	1.505	0.001	1.000	0.000	1.200	0.001	1.217	0.001	0.875	0.001
BASIL-MB	1.252	0.001	1.310	0.001	0.870	0.001	1.000	0.000	1.017	0.001	0.754	0.001
C-pCASL-MB	1.251	0.001	1.302	0.002	0.867	0.001	0.998	0.001	1.000	0.000	0.750	0.001
SRR-pCASL-MB	1.674	0.001	1.748	0.002	1.153	0.001	1.371	0.001	1.389	0.001	1.000	0.000

using joint motion estimation clearly outperformed the BASIL reference method in terms of the motion component RMMSE, with C-pCASL (without and with MB) performing best. Although RMMSE values for C-pCASL are lower than for SRR-pCASL, this does not result in lower $\overline{rRMSE}$ values, indicating that the benefits of a SRR acquisition with rotated slice-encoding and low through-plane resolution, i.e. more optimal BS and more constant PLD across slices, can outplay small inaccuracies/imprecision in motion estimation. The effect of an improved estimation of motion parameters is also visible from Fig. 9, where C-pCASL and SRR-pCASL, without and with the use of MB, result in a narrower distribution (i.e. better precision) and a higher number of voxels that match the ground truth values (i.e. better accuracy), compared to BASIL.

Finally, as can be seen from Table 6, which summarizes the overall SNR gains between the different methods for the simulation experiment with motion, SRR-pCASL outperformed C-pCASL and C-pCASL-MB. However, BASIL and BASIL-MB outperformed the proposed approach in terms of SNR of the estimated CBF map, with a maximal SNR gain for when BASIL was combined with MB. The increased SNR of BASIL may be attributed to the increase in spatial regularization as a result of its adaptive smoothing prior, which also explains the increased precision (lower $\overline{rSTD}$) and reduced accuracy (higher $\overline{arBias}$) in Table 6. To further support this observation and indicate the increased smoothness in the reconstruction results of BASIL, particularly for gray matter, Fig. S8 of the supplementary material shows orthogonal slice views with zoomed close-ups of the HR CBF maps estimated with the different approaches, compared to the ground truth CBF map as a reference.

4.2. Real data experiment

Fig. 10 shows orthogonal mid-slice views of an HR-MB 2D EPI control image acquired with high through-plane resolution ($3 \times 3 \times 3$ mm^3) and MB, and an LR 2D EPI control image with low through-plane resolution ($3 \times 3 \times 12$ mm^3) acquired with a slice orientation angle of 0°, corresponding with the acquisition settings summarized in Table 2. Fig. 10 also shows the HR CBF map estimates obtained with

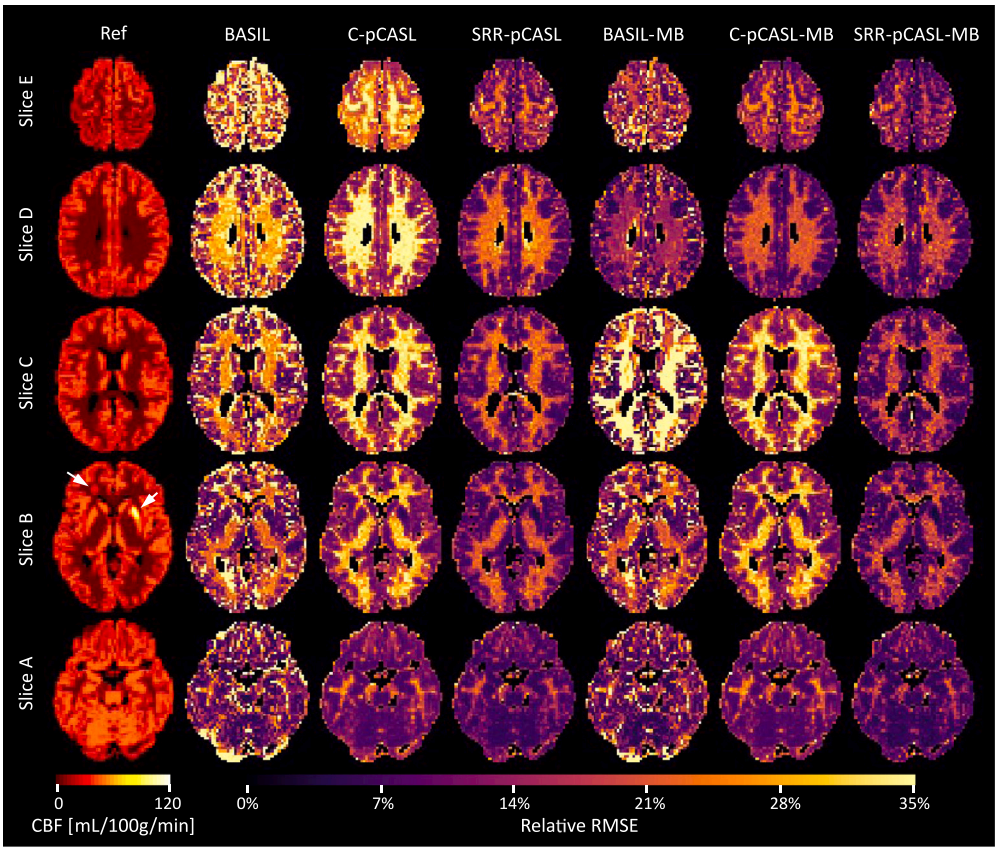

Fig. 7. Relative RMSE maps for CBF, calculated from the reconstruction results of the whole brain simulation experiments **with motion**. For each method, five transverse slices are shown, corresponding with the slice letter convention in Fig. 5. Overall relative RMSE values are summarized in Table 4. The numerical ground truth CBF map is shown in column 1. Both hyperperfusion lesions are indicated by white arrow marks in slice B of this ground truth CBF map.

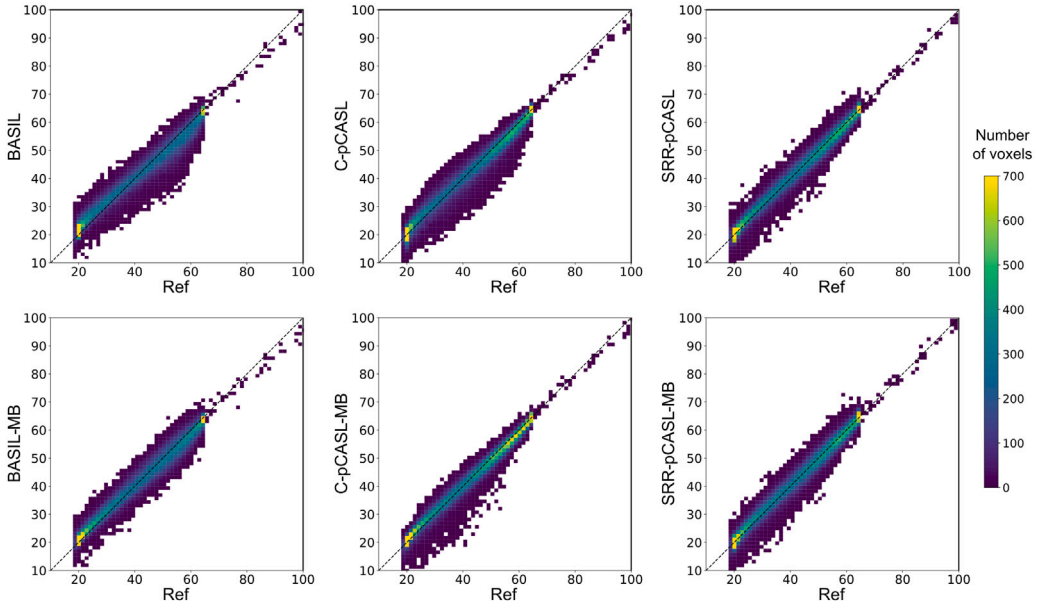

Fig. 8. 2D histograms between reference values and estimated values for all methods, as assessed by the whole brain simulation experiment **without motion**. CBF values are given in mL/100 g/min. The dashed line represents identity. Points below correspond to underestimation and points above to overestimation, compared to the reference value. For each method, values were averaged over the $N_{MC} = 100$ estimates.

BASIL-MB, C-pCASL-MB, and SRR-pCASL, respectively. Note that for the LR 2D EPI *in vivo* data set, SRR-pCASL successfully recovered the fine details from the set of LR images.

In addition, a series of transverse slices at different locations in the brain of the estimated HR quantitative CBF maps is shown in Fig. 11 for BASIL-MB, C-pCASL-MB, and the proposed SRR-pCASL. The

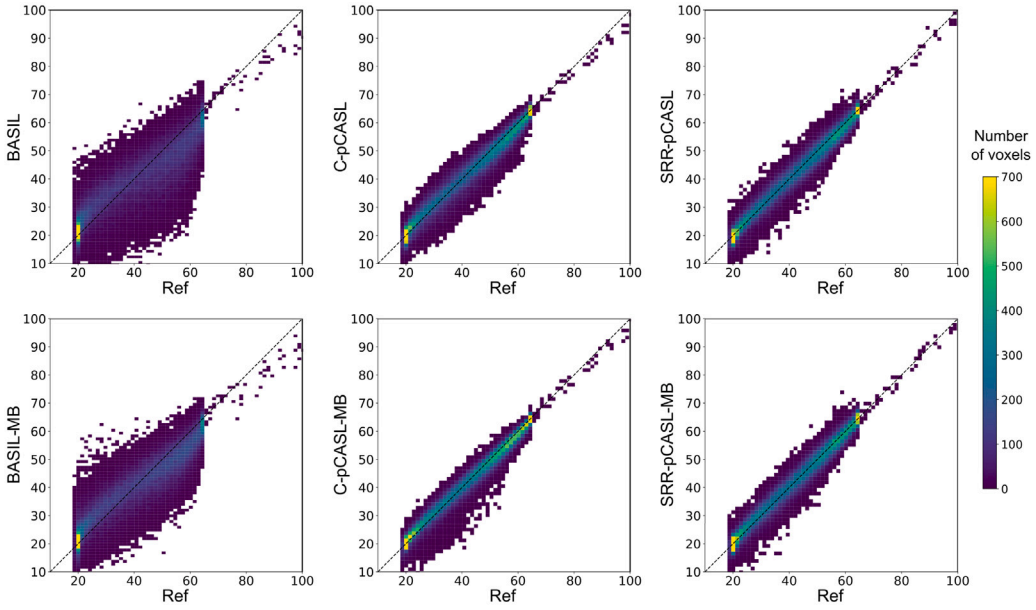

Fig. 9. 2D histograms between reference values and estimated values for all methods, as assessed by the whole brain simulation experiment **with motion**. CBF values are given in mL/100 g/min. The dashed line represents identity. Points below correspond to underestimation and points above to overestimation, compared to the reference value. For each method, values were averaged over the $N_{MC} = 100$ estimates.

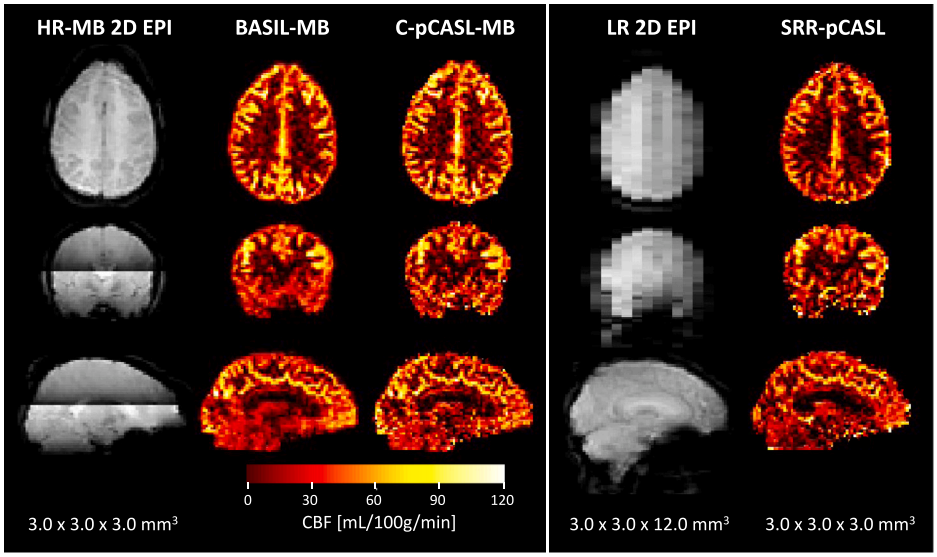

Fig. 10. Orthogonal slice views for the real data experiment showing an HR-MB 2D EPI control image acquired with high through-plane resolution ($3 \times 3 \times 3$ mm^3) and multiband (first column), and a LR 2D EPI control image with low through-plane resolution ($3 \times 3 \times 12$ mm^3) corresponding with a slice orientation angle of 0° (column 4), compared with the HR CBF map estimates obtained with BASIL-MB (second column), C-pCASL-MB (third column), and SRR-pCASL (column 5), respectively.

Table 6
The overall SNR gain ($\overline{\Gamma}_{X,Y}$) with standard error (SE) between reconstruction methods as assessed by the whole brain simulation experiment **with motion**, calculated over the $N_{MC} = 100$ reconstruction results for CBF mapping. Note that row labels refer to method X, while column labels refer to method Y, in line with the definition of $\overline{\Gamma}_{X,Y}$ in Section 3.1.3.

$\overline{\Gamma}_{X,Y}$	BASIL		C-pCASL		SRR-pCASL		BASIL-MB		C-pCASL-MB		SRR-pCASL-MB	
	Value	SE	Value	SE	Value	SE	Value	SE	Value	SE	Value	SE
BASIL	1.000	0.000	1.872	0.003	1.273	0.002	0.888	0.001	1.537	0.003	1.086	0.002
C-pCASL	0.589	0.001	1.000	0.000	0.694	0.001	0.497	0.001	0.830	0.001	0.592	0.001
SRR-pCASL	0.863	0.001	1.489	0.001	1.000	0.000	0.719	0.001	1.207	0.001	0.849	0.001
BASIL-MB	1.253	0.002	2.203	0.003	1.487	0.002	1.000	0.000	1.741	0.002	1.252	0.002
C-pCASL-MB	0.758	0.001	1.291	0.001	0.874	0.001	0.608	0.001	1.000	0.000	0.734	0.001
SRR-pCASL-MB	1.049	0.002	1.810	0.002	1.210	0.001	0.863	0.001	1.445	0.001	1.000	0.000

locations of these transverse slices are highlighted on a coronal view of the CBF map reconstructed with BASIL-MB in Fig. 5 (bottom left). As indicated in Fig. 5, slices A and B correspond with later acquired slices in the first MB segment for BASIL-MB and C-pCASL-MB, while

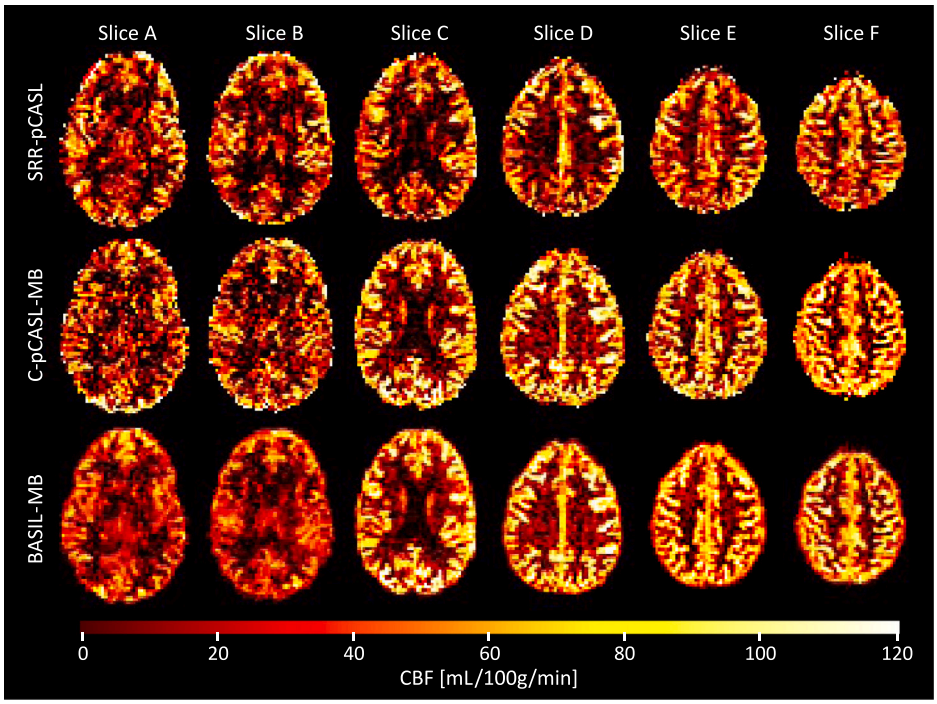

Fig. 11. Transverse slices at different locations in the brain of the estimated HR ($3 \times 3 \times 3$ mm^3) CBF maps for the different real data approaches. In the first row the estimated CBF map is shown for the proposed SRR-pCASL on the LR dataset (SRR-pCASL), and in the following rows the estimated CBF map is shown for C-pCASL on the HR dataset with multiband factor 2 (C-pCASL-MB), and BASIL on the HR dataset with multiband factor 2 (BASIL-MB), respectively. The CBF maps estimated with SRR-pCASL all have comparable CBF values, which reflects the relative uniformity in average SNR throughout all regions in the brain as a consequence of acquiring the LR images with a rotational acquisition strategy. C-pCASL-MB and BASIL-MB, on the other hand, suffer from low SNR in the posterior slices of the first multiband segment (Slice A and B) due to longer effective PLDs and limited background suppression. Slice positions correspond with those given in Fig. 5.

the other four slices are acquired relatively early in the second MB segment. When comparing the different methods, two aspects stand out. First, as can be observed in Fig. 11, the HR CBF maps reconstructed using SRR-pCASL, C-pCASL-MB and BASIL-MB are comparable in terms of absolute values and visualized anatomical structures. This clearly demonstrates the feasibility of combining SRR with single-PLD pCASL. Second, the reconstructed slices shown in Fig. 11 for the proposed SRR-pCASL approach all have comparable CBF values, reflecting the relative uniformity in SNR throughout all regions in the brain. The CBF maps obtained from the conventional HR MS data using C-pCASL-MB and BASIL-MB, on the other hand, clearly suffer from low SNR in the superior slices of the first MB segment (slices A and B in Fig. 11). For these slice locations, the proposed SRR-pCASL outperforms C-pCASL-MB and BASIL-MB in terms of reconstruction quality of the underlying anatomy.

As stated above, simulation experiments were performed for BASIL-MB and C-pCASL-MB, mimicking the same MB factor of 2 as in the real data HR pCASL experiment. Note that the stability of the CBF values across slices in SRR-pCASL (see Fig. 11) is consistent with the uniform RMSE of CBF estimation from LR MS data shown in the simulation experiment (see Fig. 6). Furthermore, the higher quality of the CBF map obtained using SRR-pCASL compared to that of BASIL-MB or C-pCASL-MB in regions of the brain that were imaged last within the MB segment (see the first two slices shown in Fig. 11) matches with the difference in RMSE of CBF estimation between both methods in those same regions as predicted in the simulation experiment (see Fig. 6). While it is difficult to compare a qualitative assessment (real data) with a quantitative measurement of RMSE (simulation data), it is reasonable to assume both effects are correlated. It serves as an indication of the validity of the simulation experiment.

5. Discussion

In this work, we introduced a model-based SRR framework for single-PLD pCASL MRI. The framework, which integrates inter-image motion estimation, provides direct whole brain 3D isotropic high resolution CBF mapping from a set of 2D multi-slice control-label image pairs with a low through-plane resolution and slice orientations that are pair-wise rotated around a common phase encoding axis. Simulation and real data results showed that this SRR acquisition strategy enables improved CBF mapping compared to the conventional 2D MS single-PLD pCASL acquisition scheme in which control-label image pairs are directly acquired at the target isotropic resolution with equal acquisition settings for each image pair, while using the same scan time. Our findings are discussed in more detail below.

5.1. Differences with existing techniques

We would like to point out that this work differs noticeably from another multi-image super-resolution resolution study for (pC)ASL, presented by Shou et al. (2021). In that work, the SLIce Dithered Enhanced Resolution (SLIDER) super-resolution technique proposed by Setsompop et al. (2015) is integrated with 2D SMS pCASL and a constrained slice-dependent background suppression (CSD-BS) scheme (Shao et al., 2018). Our approach improves upon the method presented by Shou et al. (2021) in various aspects. First, SLIDER relies on sub-voxel spatial shifts in the slice direction, whereas in our approach the slice orientations are rotated around the phase-encoding axis, which yields a more effective sampling of the k-space (Plenge et al., 2012). Previous studies that compared translational (i.e., sub-voxel shift) and rotational SRR schemes confirmed the superiority of the latter (Shilling et al., 2009; Nicastro et al., 2022). Furthermore, unlike our method, the SLIDER-SMS pCASL method of Shou et al. (2021) does not estimate CBF directly from the LR images, nor does it integrate simultaneous motion estimation, which may introduce a bias due to error propagation. Moreover, the SLIDER-SMS pCASL method models the slice profile as a box function, whereas our SRR-PCASL method models it as a more realistic smoothed box function (Poot et al., 2010). In addition, the long total scan time and lack of motion compensating steps of

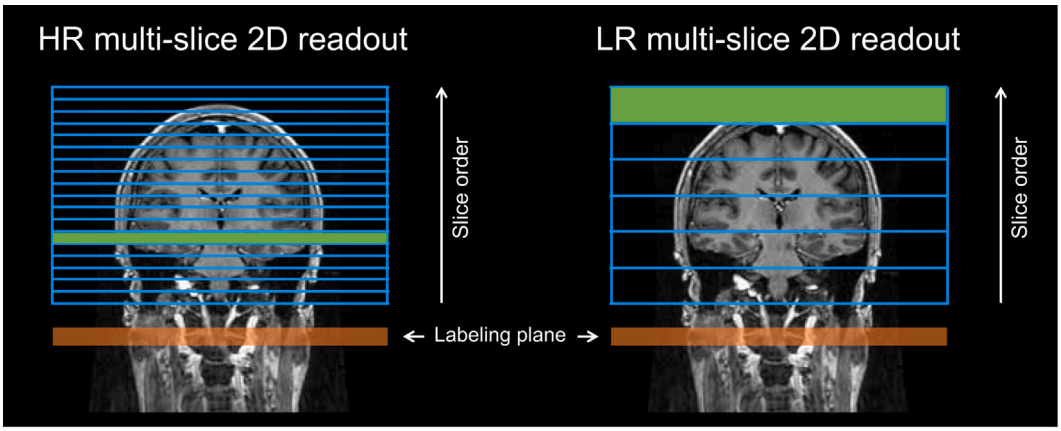

Fig. 12. A schematic representation of 2D MS readout with a high (left) and a low (right) through-plane resolution, both with an ascending acquisition order, as recommended for ASL (Alsop et al., 2015). Assuming the acquisition of an HR and an LR slice take up the same amount of scan time, the highlighted slices in green in both readout schemes will have the exact same effective PLD and level of BS. Regardless of the difference in SNR due to the difference in spatial resolution, the overall shorter effective PLD and the overall higher level of BS in the LR readout scheme will result in a higher SNR of the ASL signal on average throughout the brain.

the SLIDER-SMS pCASL method increase the susceptibility to motion artifacts, which Shou et al. (2021) identify as a limitation of their study. As demonstrated in this work, the proposed SRR-pCASL framework integrates an inter-image motion model making it less susceptible to motion artifacts.

5.2. Improved CBF quantification from single-PLD pCASL data

Comparing the CBF estimation of the different approaches in the simulation experiment without motion, the proposed SRR-pCASL framework for LR MS pCASL data showed superior CBF parameter mapping RMSE compared to both C-pCASL and BASIL for processing of conventional HR MS pCASL data (see Figs. 3, 6 and Table 3). In addition, our results showed that SRR-pCASL consistently resulted in higher average SSIM and PSNR values compared to C-pCASL and BASIL (see Table 3), indicating a better perceived image quality compared to the ground truth CBF map. Next, it was also demonstrated that the SRR-pCASL acquisition strategy, when combined with a MAP estimator, provides high resolution CBF maps with a more uniform and on average higher precision than CBF maps obtained with C-pCASL and BASIL (see Table 3, Fig. 3, and Fig. S6 of the supplementary file). This increased precision can be attributed to a two-fold gain in SNR, as provided by SRR-pCASL. First, SRR images are acquired with a low through-plane resolution, which increases the SNR as signal strength scales with the slice thickness (Delbany et al., 2019). Second, using a low through-plane resolution reduces the number of slices that need to be acquired to cover the same field-of-view (FOV) compared to higher through-plane resolution. As a result, for each LR image, the average effective PLD is shorter and the average level of BS improves compared to standard 2D MS acquisitions (see Fig. 12), which boosts the SNR throughout the entire volume. By augmenting each method with a MB factor of 2, which accelerates image acquisition and hence provides a more constant and on average better BS as well as a more constant PLD across slices, the SNR gain could be further maximized resulting in an additional improvement in CBF parameter mapping precision and RMSE for each method (see Fig. S6, Fig. 6, Tables 3 and 5). As calculated from our simulations without motion, this SNR gain was maximal when SRR-pCASL was combined with MB, relative to the other methods, with the non-MB version of SRR-pCASL even outperforming the MB versions of BASIL and C-pCASL in terms of SNR gain (see Table 5). Apart from the improved SNR, and although the labeling duration and the PLD inherently account for most of the time of the pCASL sequence, another advantage of lowering the spatial resolution in SRR-pCASL readout is a reduction of the scan time of an individual image, allowing to acquire more images within a certain amount of time compared to the acquisition of images with high spatial resolution.

5.3. Joint estimation of CBF and motion parameters

Besides the potential of SRR-pCASL to improve the traditional SNR/resolution/scan-time trade-off in ASL, the integration of a motion model and the single-PLD quantification model in the proposed SRR-pCASL reconstruction framework allows motion parameters and CBF parameters to be estimated directly and simultaneously. As such, a conventional two-step approach is avoided where HR perfusion-weighted images are reconstructed prior to voxel-wise quantification of CBF values. This benefit of the joint estimation of the motion and CBF parameters to avoid propagating errors originating from pre-registration routines (Beirinckx et al., 2022), was confirmed in the simulation experiment with motion, where it was shown that the proposed framework using joint motion estimation outperformed BASIL with FSL's *mcflirt* as a pre-registration routine in terms of motion component RMMSE (see Table 4). We also observed slightly better RMMSE values for C-pCASL than for SRR-pCASL, even when both approaches used the same Bayesian optimization framework with the same tolerance settings and regularization parameter selection. This may be the result of a combination of factors including cost function complexity, i.e. large-angle rotations are involved the SRR-pCASL forward model to compensate for the rotational acquisition, and sub-optimal hyper-parameter selection, but further research is required to investigate this discrepancy. Nevertheless, SRR-pCASL consistently resulted in lower CBF mapping RMSE values compared to C-pCASL in the simulations with motion (see Figs. 4, 7, and Table 4), indicating that the benefits of an SRR acquisition with rotated slice-encoding direction and low through-plane resolution, i.e. more optimal BS and more constant PLD across slices, provides a gain in precision that can compensate for small remaining inaccuracies in motion estimation compared to C-pCASL.

Although a thorough evaluation of BASIL and FSL's *mcflirt* was not the main scope of this work, it is worth emphasizing that default usage of these tools on motion corrupted pCASL data should be done with some precaution. As discussed in section S1.2 of the supplementary material, for one control-label image pair of the simulated HR pCASL data sets corrupted with realistic motion, we noticed consistent outliers in the motion parameter component estimation that resulted from the pre-registration routine using *mcflirt*. This forced us to consider this image pair as an outlier and to discard it from the CBF quantification using BASIL. The obligatory use of outlier correction steps, and the added question on the basis of which criteria such correction steps should be evaluated, constitutes another unnecessary step towards accurate CBF quantification. The advantage of estimating CBF and motion parameters in a single integrated approach without any form of outlier correction, as proposed in this work, offers clear added value in that respect.

Further, we also observed an increased adaptive smoothing of BASIL in the simulations with motion, which resulted in an increased rSTD precision measure for BASIL (see Fig. 4, Fig. S10, and Table 4). As a result, BASIL and BASIL-MB outperformed the proposed approaches in terms of SNR gain (see Table 6). However, as indicated by our results, this over-smoothing of BASIL resulted in a significant reduction in accuracy, as confirmed by the arBias measure (see Fig. 4, Fig. S9, and Table 4), and a significant deterioration of BASIL in terms of RMSE compared to the simulation experiment without motion (see Fig. 7). In conclusion, similar to the simulations without motion, SRR-pCASL clearly outperformed BASIL and C-pCASL in terms of overall RMSE (see Figs. 4, 7 and Table 4).

Following the extensive simulation studies, the SRR-pCASL framework was also validated on *in vivo* brain data, and compared to a single-PLD pCASL experiment on conventional pCASL data acquired with MB directly at HR (see Table 2). When comparing SRR-pCASL to the conventional HR pCASL experiment, two aspects stand out. First, the CBF maps reconstructed using SRR-pCASL (Fig. 11, top row), are comparable in terms of visualized anatomical structures to the CBF maps obtained from the conventional MS data using BASIL (Fig. 11, bottom row), and C-pCASL (Fig. 11, middle row), the last two approaches using data directly acquired at HR. Second, in certain slices (i.e. slices A–B of Fig. 11), SRR-pCASL appears to even outperform the conventional HR pCASL experiment in terms of reconstructing the underlying anatomy. This is a direct consequence of the benefit of acquiring LR data for SRR-pCASL in terms of SNR. Furthermore, the reconstructed slices of the CBF map shown in Fig. 11 for the SRR-pCASL experiment all have comparable signal intensities. This reflects the relative uniformity in average SNR throughout all regions in the brain related to the SNR benefits of acquiring LR pCASL images while using a rotational acquisition strategy. For the CBF map obtained from the conventional HR MS data, slices A–B shown in Fig. 11 clearly suffer from the low SNR due to long effective PLDs and limited BS. Similar as observed in the simulation experiment with motion, the adaptive regularization of BASIL-MB compensates for the low SNR by over-smoothing these slices A–B of the estimated CBF map, which were both acquired at the end of the first multiband (see Fig. 5). In comparison to BASIL-MB, such an over-smoothing effect was not observed in the CBF maps reconstructed with C-pCASL-MB (which uses a Laplacian prior) from the same conventional HR pCASL data set, where higher CBF intensities in the first multiband could be observed (see the coronal and sagittal views in Fig. 10). Moreover, the stability of the CBF values across slices for SRR-pCASL (see Fig. 11) is consistent with the uniform precision of CBF estimation from LR MS data using SRR-pCASL shown in the simulation experiment (see e.g. Fig. 4 and Fig. S10). Furthermore, the higher quality of the CBF map obtained from the SRR-pCASL experiment compared to that of the HR ASL experiment in regions of the brain that were imaged latest within the multiband segment (see the first two slices shown in Fig. 11) matches with the difference in RMSE of CBF estimation between both methods in those same regions as predicted in the simulation experiment (see Fig. 7). While it is difficult to compare a qualitative assessment (real data) with a quantitative measurement (simulation data), it is reasonable to assume both effects are correlated. It serves as an indication of the validity of the simulation experiment. Moreover, a qualitatively comparable CBF parameter mapping occurs for C-pCASL compared to BASIL, clearly indicative of the validity of using C-pCASL as a benchmark against SRR-pCASL in our *in vivo* experiment. Finally, it is worth noting that a closer inspection of Figs. 10–11 reveals apparently lower WM CBF values in the maps reconstructed with SRR-pCASL compared to the maps reconstructed with the other methods. Further research is recommended to explain this observation.

5.4. Model assumptions and prospective extensions

It is worth highlighting that the proposed SRR framework is generic as other ASL models can be incorporated analogously. The current framework adopts the CBF quantification model prescribed by Alsop et al. (2015), which assumes that all labeled blood has arrived in the imaging voxel before the start of the readout (i.e., ATT from the labeling plane to the readout slice is assumed to be lower than the PLD), and has stayed intravascularly while decaying with the T1 relaxation time of blood. However, it has been shown that such model is sensitive to variations in the ATT of the labeled blood (Alsop and Detre, 1996), implying the need for sufficiently long PLD. If the PLD is shorter than the ATT, the risk of macrovascular artifacts (i.e., labeled blood in proximal arteries rather than the distal capillaries or tissue) and ASL signal void (i.e., the labeled blood has not arrived yet in distal voxels resulting in ASL signal loss in these voxels) will increase. To address such issues, future work could focus on the extension of the proposed model-based SRR framework with a (nonlinear) multi-PLD pCASL model. Such a model allows to estimate the ATT parameter to improve the accuracy of CBF estimation (Buxton et al., 1998), and has already been applied for direct CBF mapping in combination with model-based reconstruction (Maier et al., 2021). Furthermore, a preliminary phantom simulation study in which the potential of SRR with multi-PLD pCASL was explored, has already been published as a conference proceeding (Bladt et al., 2017). In such an approach, each LR MS image is characterized by a unique slice orientation as well as a unique PLD time, allowing the estimation of both CBF and ATT. However, given the nonlinear nature of the multi-PLD pCASL model as well as the increased number of parameters to be estimated, the computational cost of the optimization is expected to increase. Note, also, that although such ASL model extensions may improve the accuracy of the estimated parameter maps, the addition of extra parameters to be estimated comes at the expense of a reduced precision. Furthermore, it is often assumed that the reduction in data averaging when using multiple time point protocols (required when acquiring the data in a matched scan time with a single-PLD protocol) leads to a reduction in the precision of the CBF estimates (Alsop et al., 2015; Dai et al., 2017; Teeuwisse et al., 2014), which could outweigh the benefits of correcting for ATT effects. At this point, future work could focus on investigating to what extent this reduction in CBF precision can be compensated for by the gain in precision associated with the use of SRR-pCASL. Overall, the effects of accuracy and precision should be carefully weighed against each other.

In this work, the calibration image $\boldsymbol{\rho}$ was acquired from a separate acquisition at the target resolution, i.e., the resolution of the reconstructed $\boldsymbol{\vartheta}_{\mathrm{rCBF}}$ map, followed by a multi-modal registration step to align $\boldsymbol{\vartheta}_{\mathrm{rCBF}}$ and $\boldsymbol{\rho}$, which then allowed absolute CBF quantification via voxel-wise division of $\boldsymbol{\vartheta}_{\mathrm{rCBF}}$ and $\boldsymbol{\rho}_{\mathrm{reg}}$ to a HR CBF parameter map $\boldsymbol{\vartheta}_{\mathrm{CBF}}$. An alternative approach could be to integrate the registration with the calibration image $\boldsymbol{\rho}$ as part of the cyclic block-coordinate descent optimization scheme in Section 2.3.2, resulting in an additional set of motion parameters $\boldsymbol{\theta}_{\rho} \in \mathbb{R}^{6\times 1}$ to be estimated simultaneously with $\{\boldsymbol{\vartheta}, \boldsymbol{\theta}\}$. This approach would avoid a separate calibration step, and could reduce a potential bias from propagating registration errors. However, similar to the addition of a multi-PLD model, the effects of accuracy and precision should be carefully considered as the estimation of additional motion parameters could come at the cost of a reduced precision. Furthermore, the benefit of simultaneous estimation of $\boldsymbol{\theta}_{\rho}$ must be weighed against the extra computational cost associated with such estimation. In particular, modeling $\boldsymbol{\theta}_{\rho}$ requires the introduction of an extra (computationally intensive) image warping operator in the numerator of the single-PLD pCASL signal model in Eq. (2). While image operators $\boldsymbol{M}_{\boldsymbol{\theta}_n}$ and $\boldsymbol{G}_n$ are currently combined in one warping operation to maximize computational efficiency, an additional image warping operator for $\boldsymbol{\theta}_{\rho}$ would demand a full operator call for every forward pass in the cost function. The latter would cause a significant

increase in the computational cost of the framework. Therefore, in this work, the decision was made to consider the calibration step separately. Future work is encouraged to further investigate the impact of joint calibration on CBF quantification and computation time.

5.5. Limitations

In our current implementation, the signal in the voxels of the LR images is assumed to be Gaussian distributed, which is a valid assumption for sufficiently high SNR. The MAP estimation then becomes a least-squares optimization, which can be solved efficiently as a linear optimization problem. However, other data distributions may apply when the SNR condition is not met, or when other coil acquisition setups, e.g. using parallel imaging, are used. In that case, the log likelihood can take a nonlinear form, resulting in a nonlinear optimization problem that requires more advanced computational solvers. Future work could focus on investigating the impact on CBF estimation when other data distributions, as well as spatial and temporal variations in the noise standard deviation maps of the LR images, are used.

The comparison between the considered CBF estimation frameworks depends on the imposed prior information on the unknown parameter maps, as well as the tuning of the associated regularization weights. While the SRR-pCASL framework uses a Laplacian prior (cfr. Section 2.3.1), and regularization weights can be chosen equally for SRR-pCASL and C-pCASL, BASIL uses an adaptive non-local spatial smoothing prior based on CBF variations in the brain, without a priori user-selected regularization weights. In order to compare the performance of the different methods in a reliable manner, ideally, the level of regularization should be the same in all reconstructions. At the same time, tuning regularization weights of a multiple regularization parameter selection problem as proposed, remains a difficult problem. In the current work, the hyper-parameters of the prior distributions in Eq. (8) were heuristically selected to be minimally intrusive in the reconstruction, balancing the trade-off between the data consistency objective and the regularization objectives of the tissue parameter maps. This approach may be sub-optimal.

A more fair comparison between SRR-pCASL, C-pCASL-MB and BASIL-MB in the real data experiments would be achieved when MB was (not) used in all experiments. One could argue that the current real data comparison was skewed in favor of the conventional HR ASL experiment, because MB was only used for HR ASL data acquisition. However, this choice was made for two reasons. On the one hand, a MB factor of 2 was used in the HR ASL experiment, as otherwise there would have been practically no ASL signal remaining in most of the upper part of the brain. As this was a proof-of-concept study, being able to verify whether the SRR-pCASL reconstructed CBF maps showed anatomical details comparable to those of BASIL-MB was more important than a true one-to-one comparison of the conventional HR ASL and SRR-pCASL experiment. On the other hand, MB was not used in the SRR-pCASL experiment, because MB acquisition required a calibration scan to be performed before acquisition of each LR image. This would have taken up too much of the available total scan time. Future work that investigates whether the SRR acquisition strategy can be combined with MB more efficiently, to allow for a more fair comparison between both strategies, is highly encouraged. As demonstrated in our simulation study without motion, the use of MB in SRR-pCASL-MB provided an additional improvement in relative RMSE of about 10% compared to SRR-pCASL, largely contributed to by the increased estimation precision.

Finally, the SRR-pCASL protocol needs to be validated on more subjects in order to demonstrate its intra- and inter-subject robustness. Ideally, data should be acquired repeatedly in individual subjects, in order to be able to determine sample standard deviations for CBF map estimates, similarly to the analysis done in simulations. This would allow to quantify the performance of SRR-pCASL and C-pCASL in more detail. In addition, CBF map estimates obtained using our SRR-pCASL method for 2D MS readout should be further compared with results obtained using recommended segmented 3D readout schemes. We anticipate that motion robustness and through-plane blurring are two effects where the proposed SRR-pCASL method with joint motion estimation offers potential improvements over segmented 3D readout.

5.6. Anticipated clinical impact and future perspectives

Our research also highlights some advantages that could potentially have profound clinical impact. The FOV of the LR pCASL data for SRR-pCASL provides wider coverage in the slice direction (192 mm) compared to the conventional HR data (120 mm), acquired in the same total scan time. On the one hand, this wider coverage is required for SRR because the entire brain has to be within the FOV for each rotation angle. On the other hand, it offers a potential advantage to applications where such large coverage is required. An advantage, for example, is that the labeling plane can be scanned, which is not standard for conventional ASL acquisitions. Directly visualizing the labeling plane can offer valuable information for off-resonance correction schemes that investigate B0 field inhomogeneity distortions in the labeling plane (Berry et al., 2019). In addition, the larger coverage would potentially allow perfusion quantification in deep brain structures such as the brain stem, cerebellum, and even the spinal cord (Shou et al., 2021). These brain structures are important nodes of the structural and functional networks of the human brain. However, to date, very few perfusion measurements have been performed in these structures.

Further, we anticipate that the combination of a rotated SRR acquisition strategy with MB imaging (also known as SMS) offers great promise to overcome some of the limitations of ultra-high-field (UHF; 7T and higher) ASL techniques (Teeuwisse et al., 2010). The added value of such a combined acquisition strategy seems twofold. First, image SNR increases both with field strength (Gardener et al., 2009), and due to acquisition with low through-plane resolution and increased effectiveness of BS associated with SRR and MB, as clearly demonstrated in this work (see also Fig. 12). Second, the combination of SRR with MB offers an attractive approach to increase the currently limited spatial coverage at these higher field strengths (Ivanov et al., 2017), since both several spatially distributed imaging slices are excited and the through-plane resolution of each slice is increased.

It is worth discussing whether the proposed SRR approach can be extended to pCASL with 3D readout. Super-resolution reconstruction is conventionally defined as the recovery of high-frequency components corrupted by aliasing (Kang and Chaudhuri, 2003). In 2D multi-slice imaging, aliasing occurs in the through-plane direction, which facilitates SRR. However, there is consensus that super-resolution in MRI is not achievable in-plane (Greenspan et al., 2002; Scheffler, 2002; Plenge et al., 2012), nor in true 3D acquisitions, since the Fourier encoding scheme excludes aliasing in frequency and phase encoding directions. Notwithstanding the aliasing condition, the proposed estimation framework is fully compatible with 3D pCASL data (provided that the slice selection profile is turned off). In that case, the reconstruction will mainly benefit from the joint estimation of CBF and motion parameters, while the potential resolution gain is expected to be marginal. At the same time, 3D readout remains subject to several disadvantages, including spatial blurring due to T2 decay and a high sensitivity to (intra-scan) motion. These disadvantages could complicate resolution enhancement using LR 3D ASL scans. In particular, it is crucial that such effects are included in the forward model for (iterative) reconstruction which connects the ground truth CBF map to the observed data.

Finally, the combination of the proposed SRR acquisition strategy with alternative ASL labeling approaches, such as Hadamard time encoding (in the context of multi-PLD pCASL) (Teeuwisse et al., 2014), and velocity selective encoding (Qin et al., 2022), seems worth investigating and is suggested as a possible extension of this work.

6. Conclusion

This work has introduced a model-based super-resolution reconstruction framework for single-PLD pCASL MRI, building on a joint Bayesian estimation framework that aims to estimate motion-corrected 3D isotropic high-resolution quantitative CBF maps from a set of 2D multi-slice control-label image pairs acquired with low through-plane resolution and rotated slice-encoding direction. The framework has been validated in synthetic whole brain simulations and on *in vivo* human brain data, demonstrating successful CBF quantification while providing a more uniform distribution of PLD, improved SNR, and increased effectiveness of BS compared to conventional 2D MS readout with ascending slice order and isotropic resolution in the same scan time, even when multiband is applied in the latter. By improving upon existing disadvantages of 2D MS readout, the proposed framework provides a promising alternative to the recommended segmented 3D readout schemes, which to date remain sensitive to inter-shot motion and through-plane blurring due to T2 decay along the long echo trains.

CRediT authorship contribution statement

Quinten Beirinckx: Conceptualization, Formal analysis, Investigation, Methodology, Software, Validation, Visualization, Writing – original draft, Writing – review & editing. **Piet Bladt:** Investigation, Methodology, Software, Writing – review & editing. **Merlijn C.E. van der Plas:** Investigation. **Matthias J.P. van Osch:** Resources, Supervision, Writing – review & editing. **Ben Jeurissen:** Methodology, Software, Writing – review & editing. **Arnold J. den Dekker:** Conceptualization, Formal analysis, Methodology, Supervision, Writing – review & editing. **Jan Sijbers:** Conceptualization, Formal analysis, Methodology, Resources, Supervision, Writing – review & editing.

Declaration of competing interest

None.

Data and code availability

In vivo data used in this work can be shared upon formal request by contacting the corresponding author, and a data sharing agreement should be signed by all parties. The plan is to release the code for the proposed SRR-pCASL framework via an open source GitHub repository. The data and code sharing adopted by the authors comply with the requirements of the funding body or institute, and with the institutional ethics approval. Parts of the data are confidential and additional ethical approval may be needed for re-use.

Acknowledgments

The authors gratefully acknowledge support from the Research Foundation Flanders, Belgium (FWO) through project funding G084217N, G096324N and 1S69918N, and from the Belgian Science Policy Office-Prodex. Furthermore, the authors would like to thank Sophie Schmid and Wouter M. Teeuwisse for their help during the acquisition of the *in-vivo* datasets.

Appendix A. Slice-dependent PLD

When using a conventional 2D multi-slice readout strategy for pCASL with subsequently acquired slices, distal slices will have longer effective PLDs than proximal slices. This slice-dependent effective PLD can be represented using a function that maps each ordered triplet of HR grid coordinates to a voxel value holding the effective PLD, i.e., $\mathbf{PLD}: D \subset \mathbb{N}_0^3 \mapsto \mathbb{R}$, where $D = \{(i,j,k) \mid i = 1,\dots,u;\ j = 1,\dots,v;\ k = 1,\dots,w;$ and $u,v,w \in \mathbb{N}_0\}$, with $N_r = u \times v \times w$. Assuming that the base PLD value, $\mathrm{PLD}_{\mathrm{base}}$, increases by a multiple of the slice readout time, t_{read}, for ascending slices in a conventional 2D multi-slice pCASL acquisition, the (i,j,k)th voxel value of **PLD** is defined as:

$$\mathrm{PLD}(i,j,k) = \mathrm{PLD}_{\mathrm{base}} + t_{\mathrm{read}} \cdot h(k) \quad , \tag{A.1}$$

with $\boldsymbol{h}: \mathbb{N}_0 \mapsto \mathbb{N}$, $\boldsymbol{h} = \{h(k) \mid k = 1,\dots,w$ and $w \in \mathbb{N}_0\}$, a function that defines the integer multiplication factor for the kth slice of **PLD**:

$$h(k) = \frac{1}{\zeta}\left[(k-1) \bmod \varrho - ((k-1) \bmod \varrho) \bmod \zeta\right], \tag{A.2}$$

where ζ is equal to the anisotropy factor, defined as the ratio of the through-plane resolution to the in-plane resolution, and with ϱ the number of HR slices per band, i.e. the ratio of the total number of HR slices to the multiband factor. The application of function $\boldsymbol{h}$ is illustrated in Fig. A.1.

When using a SRR acquisition strategy, 2D multi-slice images are acquired with anisotropic voxel size, where each LR image samples the HR scene in a distinct fashion to ensure that the acquired data contains complementary information about the HR image or HR parameter maps to be reconstructed. In this work, the LR images are acquired with varying slice-encoding directions (Fig. 1). Consequently, effective PLD values will vary according to the assumed slice-encoding direction of each LR image. Under the assumption that no labeling of cerebral blood is present at an infinitely long PLD, the effective PLD values of the nth HR pCASL image $\boldsymbol{r}_n$ can be modeled using a function $\mathbf{PLD}_n = \{\mathrm{PLD}_{nj}\}_{j=1}^{N_r} \in \mathbb{R}^{N_r \times 1}$:

$$\mathbf{PLD}_n = \begin{cases} \infty, & \text{if } n \text{ is odd} \\ \boldsymbol{M}_{\theta_n}^{-1}\boldsymbol{G}_n^{-1}\mathbf{PLD}, & \text{if } n \text{ is even} \end{cases} \quad , \tag{A.3}$$

where $\boldsymbol{M}_{\theta_n}^{-1} \in \mathbb{R}^{N_r \times N_r}$ and $\boldsymbol{G}_n^{-1} \in \mathbb{R}^{N_r \times N_r}$ denote the exact inverse warping operators of operators $\boldsymbol{M}_{\theta_n}$ and $\boldsymbol{G}_n$, respectively, which are required to anticipate image warping in the super-resolution forward model in Eq. (1). Note that in this work, similar to Ramos-Llordén et al. (2017) and Beirinckx et al. (2022), image warping is implemented very efficiently with Fast Fourier Transforms (FFT). With the FFT approach, $\boldsymbol{M}_{\theta_n}$ (or $\boldsymbol{G}_n$) can be shown to be unitary, which means that its inverse $\boldsymbol{M}_{\theta_n}^{-1}$ is equal to $\boldsymbol{M}_{\theta_n}^{H} \in \mathbb{R}^{N_r \times N_r}$, where the superscript H denotes the adjoint or Hermitian conjugate. Hence, the warping operator $\boldsymbol{M}_{\theta_n}$ is easily reversible, i.e. when applied to an image, the image can be retrieved by applying $\boldsymbol{M}_{\theta_n}^{H}$ to the output of this operation.

Appendix B. Background suppression

Background suppression (BS) can be used to increase the SNR of the ASL signal by suppressing the physiological noise component that

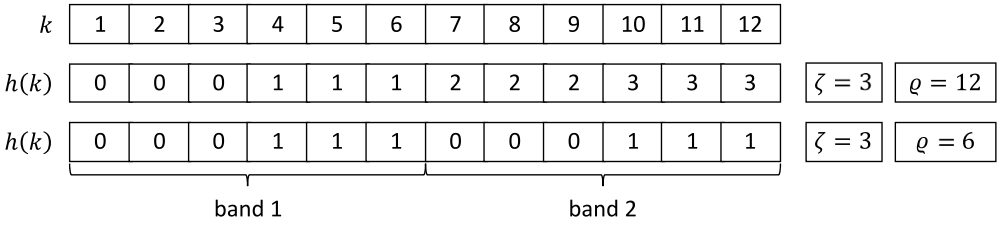

Fig. A.1. Illustration of Eq. (A.2) where function $\boldsymbol{h}$ operates on a 1-dimensional HR grid vector $k = 1,\dots,12$, oriented along the slice-encoding dimension, using an anisotropy factor $\zeta = 3$, with $\varrho = 12$ (i.e., no SMS), and with $\varrho = 6$ HR slices per band when SMS with multiband factor 2 is modeled.

scales with the signal intensity in the label and control images. BS can be achieved using a combination of a saturation pulse and a certain number of inversion pulses applied to the imaging volume (Garcia et al., 2005; Maleki et al., 2012). By timing these inversion pulses correctly with the readout excitation, the longitudinal magnetization of the static background tissue will pass through zero at the time of readout. For imaging methods that employ a single excitation per repetition time (TR), such as the segmented 3D approaches, BS can be highly effective, as the null point of the magnetization can be timed to coincide with the excitation pulse. However, in 2D multi-slice readout for pCASL, used for SRR, an excitation pulse is used for each individual slice and slices are acquired subsequently resulting in different slice acquisition times. As a result, BS can be optimal for one slice, but is progressively less efficient for other slices.

Under the assumption that BS is perfect for the first acquired slice and that signal in subsequent slices recovers towards equilibrium with T_1 of tissue, the slice-dependent variation of optimal inversion time points for BS in a conventional 2D multi-slice pCASL acquisition with ascending slice order, can be represented as a function $\mathbf{TI} : D \subset \mathbb{N}_0^3 \mapsto \mathbb{R}$, where $D = \{\,(i,j,k) \mid i = 1,\dots,u;\ j = 1,\dots,v;\ k = 1,\dots,w;\ \text{and } u,v,w \in \mathbb{N}_0\,\}$, with $N_r = u \times v \times w$. Similar to the definition of slice-dependent PLD values in Eq. (A.1), it is assumed that inversion times increase by a multiple of the readout time per slice for ascending slice numbers. As such, the (i,j,k)th voxel value of $\mathbf{TI}$ is defined as:

$$\mathrm{TI}(i,j,k) = T_1(i,j,k) \cdot \ln(2) + t_{\mathrm{read}} \cdot h(k) \quad , \tag{B.1}$$

with $\boldsymbol{h}$ following the same definition as in Eq. (A.2).

For a SRR acquisition, the optimal inversion times for perfect background suppression of each slice will depend on the corresponding slice-encoding direction of each separate acquisition. Therefore, for each HR pCASL image $\boldsymbol{r}_n$, the corresponding $\mathbf{TI}_n = \{\mathrm{TI}_{nj}\}_{j=1}^{N_r} \in \mathbb{R}^{N_r \times 1}$ can be modeled as:

$$\mathbf{TI}_n = \boldsymbol{M}_{\theta_n}^{-1} \boldsymbol{G}_n^{-1} \mathbf{TI} \quad . \tag{B.2}$$

Next, let $\boldsymbol{b}_n = \{b_{nj}\}_{j=1}^{N_r} \in \mathbb{R}^{N_r \times 1}$ represent a vector that models the T_1 relaxation factor for inversion-recovery nulling for BS, assuming TR $\gg T_1$ and a perfect 180° RF inversion pulse (Barral et al., 2010), with

$$b_{nj} = 1 - 2 \cdot \exp\left(-\frac{\mathrm{TI}_{nj}}{T_{1,j}}\right). \tag{B.3}$$

Then, Eq. (4) can be extended to include the effect of background suppression:

$$r_{nj} = \begin{cases} r_{1,j} b_{nj}, & \text{if } n \text{ is odd} \\ r_{1,j} b_{nj} - \Delta r_{nj}, & \text{if } n \text{ is even.} \end{cases} \tag{B.4}$$

Appendix C. Linear forward model

It follows from Eq. (4) that the HR images $\boldsymbol{r}_n$ can be modeled as a linear function of the parameter vector $\boldsymbol{\vartheta} = [\boldsymbol{r}_1^T\ \boldsymbol{\vartheta}_{\mathrm{rCBF}}^T]^T \in \mathbb{R}^{2N_r \times 1}$:

$$\boldsymbol{r}_n(\boldsymbol{\vartheta}) = \boldsymbol{A}_n \boldsymbol{\vartheta} \tag{C.1}$$

where $\boldsymbol{A}_n \in \mathbb{R}^{N_r \times 2N_r}$ represents the block matrix operator:

$$\boldsymbol{A}_n = \begin{cases} \begin{bmatrix} \boldsymbol{I}_{N_r} & \boldsymbol{0}_{N_r} \end{bmatrix}, & \text{if } n \text{ is odd} \\ \begin{bmatrix} \boldsymbol{I}_{N_r} & \mathrm{diag}(\boldsymbol{v}_n) \end{bmatrix}, & \text{if } n \text{ is even} , \end{cases} \tag{C.2}$$

whose matrix elements are given by

$$\boldsymbol{A}_n = \begin{cases} \begin{bmatrix} 1 & 0 & \dots & 0 & 0 & 0 & \dots & 0 \\ 0 & 1 & \ddots & \vdots & 0 & 0 & \ddots & \vdots \\ \vdots & \ddots & \ddots & 0 & \vdots & \ddots & \ddots & 0 \\ 0 & \dots & 0 & 1 & 0 & \dots & 0 & 0 \end{bmatrix}, & \text{if } n \text{ is odd} \\ \begin{bmatrix} 1 & 0 & \dots & 0 & v_{n,1} & 0 & \dots & 0 \\ 0 & 1 & \ddots & \vdots & 0 & v_{n,2} & \ddots & \vdots \\ \vdots & \ddots & \ddots & 0 & \vdots & \ddots & \ddots & 0 \\ 0 & \dots & 0 & 1 & 0 & \dots & 0 & v_{n,N_r} \end{bmatrix}, & \text{if } n \text{ is even} , \end{cases} \tag{C.3}$$

with $\boldsymbol{I}_{N_r} \in \mathbb{R}^{N_r \times N_r}$ the identity matrix, $\boldsymbol{0}_{N_r} \in \mathbb{R}^{N_r \times N_r}$ the zero matrix, $\mathrm{diag}(\boldsymbol{v}_n) \in \mathbb{R}^{N_r \times N_r}$ a diagonal matrix with the elements of $\boldsymbol{v}_n = \{v_{nj}\}_{j=1}^{N_r} = \{-\Delta r_{nj}/\vartheta_{\mathrm{rCBF},j}\}_{j=1}^{N_r} = \left\{-\delta^{-1} \exp\left(-\mathrm{PLD}_{n,j}/T_{1b}\right)\right\}_{j=1}^{N_r} \in \mathbb{R}^{N_r \times 1}$ on its diagonal. Consequently, when combining Eq. (C.1) with the linear SRR forward model operators in Eq. (1), the overall forward model in SRR-pCASL remains linear, which allows for efficient solving of (P.1) using linear optimization routines.

Appendix D. Supplementary materials

Supplementary material related to this article can be found online at https://doi.org/10.1016/j.neuroimage.2024.120506.

References

Alsop, D.C., Detre, J.A., 1996. Reduced transit-time sensitivity in noninvasive magnetic resonance imaging of human cerebral blood flow. J. Cereb. Blood Flow Metab. 16 (6), 1236–1249. http://dx.doi.org/10.1097/00004647-199611000-00019.

Alsop, D.C., et al., 2015. Recommended implementation of arterial spin-labeled perfusion MRI for clinical applications: A consensus of the ISMRM perfusion study group and the European consortium for ASL in dementia. Magn. Reson. Med. 73 (1), 102–116. http://dx.doi.org/10.1002/mrm.25197.

Bano, W., Piredda, G.F., Davies, M., Marshall, I., Golbabaee, M., Meuli, R., Kober, T., Thiran, J.P., Hilbert, T., 2020. Model-based super-resolution reconstruction of T2 maps. Magn. Reson. Med. 83 (3), 906–919. http://dx.doi.org/10.1002/mrm.27981.

Barral, J.K., Gudmundson, E., Stikov, N., Etezadi-Amoli, M., Stoica, P., Nishimura, D.G., 2010. A robust methodology for in vivo T1 mapping. Magn. Reson. Med. 64 (4), 1057–1067. http://dx.doi.org/10.1002/mrm.22497.

Beck, A., Tetruashvili, L., 2013. On the convergence of block coordinate descent type methods. SIAM J. Optim. 23 (4), 2037–2060. http://dx.doi.org/10.1137/120887679.

Beirinckx, Q., Jeurissen, B., Nicastro, M., Poot, D.H.J., Verhoye, M., den Dekker, A.J., Sijbers, J., 2022. Model-based super-resolution reconstruction with joint motion estimation for improved quantitative MRI parameter mapping. Comput. Med. Imaging Graph. 100, 102071. http://dx.doi.org/10.1016/j.compmedimag.2022.102071.

Beirinckx, Q., Ramos-Llordén, G., Jeurissen, B., Poot, D.H.J., Parizel, P.M., Verhoye, M., Sijbers, J., den Dekker, A.J., 2020. Joint maximum likelihood estimation of motion and T1 parameters from magnetic resonance images in a super-resolution framework: a simulation study. Fund. Inform. 172, 105–128. http://dx.doi.org/10.3233/FI-2020-1896.

Berry, E.S., Jezzard, P., Okell, T.W., 2019. Off-resonance correction for pseudo-continuous arterial spin labeling using the optimized encoding scheme. NeuroImage 199, 304–312. http://dx.doi.org/10.1016/j.neuroimage.2019.05.083.

Bladt, P., Beirinckx, Q., van der Plas, M.C.E., Schmid, S., Teeuwisse, W.M., Jeurissen, B., den Dekker, A.J., Sijbers, J., van Osch, M.J.P., 2020. Super-resolution reconstruction of single-PLD pseudo-continuous ASL images. In: Proc. Intl. Soc. Mag. Reson. Med., Vol. 28. p. 3293.

Bladt, P., Beirinckx, Q., Van Steenkiste, G., Jeurissen, B., Achten, E., den Dekker, A.J., Sijbers, J., 2017. Super-resolution multi-PLD PCASL: a simulation study. Magn. Reson. Mater. Phys. Biol. Med. 30 (Suppl. 1), http://dx.doi.org/10.1007/s10334-017-0634-z.

Buxton, R.B., Frank, L.R., Wong, E.C., Siewert, B., Warach, S., Edelman, R.R., 1998. A general kinetic model for quantitative perfusion imaging with arterial spin labeling. Magn. Reson. Med. 40 (3), 383–396. http://dx.doi.org/10.1002/mrm.1910400308.

Chappell, M.A., Groves, A.R., Whitcher, B., Woolrich, M.W., 2009. Variational Bayesian inference for a nonlinear forward model. IEEE Trans. Signal Process. 57 (1), 223–236. http://dx.doi.org/10.1109/TSP.2008.2005752.

Clement, P., Petr, J., Dijsselhof, M.B.J., Padrela, B., Pasternak, M., Dolui, S., Jarutyte, L., Pinter, N., Hernandez-Garcia, L., Jahn, A., Kuijer, J.P.A., Barkhof, F., Mutsaerts, H.J.M.M., Keil, V.C., 2022. A beginner's guide to arterial spin labeling (ASL) image processing. Front. Radiol. 2, http://dx.doi.org/10.3389/fradi.2022.929533.

Coleman, T.F., Li, Y., 1994. On the convergence of reflective Newton methods for large-scale minimization subject to bounds. Math. Program. 67 (2), 189–224. http://dx.doi.org/10.1007/BF01582221.

Dai, W., Fong, T., Jones, R.N., Marcantonio, E., Schmitt, E., Inouye, S.K., Alsop, D.C., 2017. Effects of arterial transit delay on cerebral blood flow quantification using arterial spin labeling in an elderly cohort. J. Magn. Reson. Imaging 45 (2), 472–481. http://dx.doi.org/10.1002/jmri.25367.

den Dekker, A.J., Sijbers, J., 2014. Data distributions in magnetic resonance images: A review. Phys. Med. 30 (7), 725–741. http://dx.doi.org/10.1016/j.ejmp.2014.05.002.

Delbany, M., Bustin, A., Poujol, J., Thomassin-Naggara, I., Felblinger, J., Vuissoz, P.-A., Odille, F., 2019. One-millimeter isotropic breast diffusion-weighted imaging: Evaluation of a superresolution strategy in terms of signal-to-noise ratio, sharpness and apparent diffusion coefficient. Magn. Reson. Med. 81 (4), 2588–2599. http://dx.doi.org/10.1002/mrm.27591.

Fan, A.P., Jahanian, H., Holdsworth, S.J., Zaharchuk, G., 2016. Comparison of cerebral blood flow measurement with [^{15}O]-water positron emission tomography and arterial spin labeling magnetic resonance imaging: A systematic review. J. Cereb. Blood Flow Metab. 36 (5), 842–861. http://dx.doi.org/10.1177/0271678X16636393.

Fessler, J.A., Kim, D., 2011. Axial block coordinate descent (ABCD) algorithm for X-ray CT image reconstruction. In: Proc. Intl. Mtg. on Fully 3D Image Recon. in Rad. and Nuc. Med.. pp. 262–265.

Fogtmann, M., Seshamani, S., Kroenke, C., Cheng, X., Chapman, T., Wilm, J., Rousseau, F., Studholme, C., 2014. A unified approach to diffusion direction sensitive slice registration and 3-D DTI reconstruction from moving fetal brain anatomy. IEEE Trans. Med. Imaging 33 (2), 272–289. http://dx.doi.org/10.1109/tmi.2013.2284014.

Garcia, D.M., Duhamel, G., Alsop, D.C., 2005. Efficiency of inversion pulses for background suppressed arterial spin labeling. Magn. Reson. Med. 54 (2), 366–372. http://dx.doi.org/10.1002/mrm.20556.

Gardener, A.G., Gowland, P.A., Francis, S.T., 2009. Implementation of quantitative perfusion imaging using pulsed arterial spin labeling at ultra-high field. Magn. Reson. Med. 61 (4), 874–882. http://dx.doi.org/10.1002/mrm.21796.

Greenspan, H., Oz, G., Kiryati, N., Peled, S., 2002. MRI inter-slice reconstruction using super-resolution. Magn. Reson. Imaging 20 (5), 437–446. http://dx.doi.org/10.1016/s0730-725x(02)00511-8.

Groves, A.R., Chappell, M.A., Woolrich, M.W., 2009. Combined spatial and non-spatial prior for inference on MRI time-series. NeuroImage 45 (3), 795–809. http://dx.doi.org/10.1016/j.neuroimage.2008.12.027.

Hernandez-Garcia, L., Aramendía-Vidaurreta, V., Bolar, D.S., Dai, W., Fernández-Seara, M.A., Guo, J., Madhuranthakam, A.J., Mutsaerts, H., Petr, J., Qin, Q., Schollenberger, J., Suzuki, Y., Taso, M., Thomas, D.L., van Osch, M.J.P., Woods, J., Zhao, M.Y., Yan, L., Wang, Z., Zhao, L., Okell, T.W., 2022. Recent technical developments in ASL: A review of the state of the art. Magn. Reson. Med. 88 (3), 2021–2042. http://dx.doi.org/10.1002/mrm.29381.

Ivanov, D., Poser, B.A., Huber, L., Pfeuffer, J., Uludağ, K., 2017. Optimization of simultaneous multislice EPI for concurrent functional perfusion and BOLD signal measurements at 7T. Magn. Reson. Med. 78 (1), 121–129. http://dx.doi.org/10.1002/mrm.26351.

Jenkinson, M., Bannister, P., Brady, M., Smith, S., 2002. Improved optimization for the robust and accurate linear registration and motion correction of brain images. NeuroImage 17 (2), 825–841. http://dx.doi.org/10.1006/nimg.2002.1132.

Kang, M.G., Chaudhuri, S., 2003. Super-resolution image reconstruction. IEEE Signal Process. Mag. 20 (3), 19–20. http://dx.doi.org/10.1109/MSP.2003.1203206.

Krüger, G., Glover, G.H., 2001. Physiological noise in oxygenation-sensitive magnetic resonance imaging. Magn. Reson. Med. 46 (4), 631–637. http://dx.doi.org/10.1002/mrm.1240.

Liu, F., Velikina, J.V., Block, W.F., Kijowski, R., Samsonov, A.A., 2017. Fast realistic MRI simulations based on generalized multi-pool exchange tissue model. IEEE Trans. Med. Imaging 36 (2), 527–537. http://dx.doi.org/10.1109/TMI.2016.2620961.

Maier, O., Spann, S.M., Pinter, D., Gattringer, T., Hinteregger, N., Thallinger, G.G., Enzinger, C., Pfeuffer, J., Bredies, K., Stollberger, R., 2021. Non-linear fitting with joint spatial regularization in arterial spin labeling. Med. Image Anal. 71, 102067. http://dx.doi.org/10.1016/j.media.2021.102067.

Maleki, N., Dai, W., Alsop, D.C., 2012. Optimization of Background Suppression for Arterial Spin Labeling Perfusion Imaging, Vol. 25. MAGMA.

Nicastro, M., Jeurissen, B., Beirinckx, Q., Smekens, C., Poot, D.H.J., Sijbers, J., den Dekker, A.J., 2022. To shift or to rotate? Comparison of acquisition strategies for multi-slice super-resolution magnetic resonance imaging. Front. Neurosci. 16, 1044510. http://dx.doi.org/10.3389/fnins.2022.1044510.

Parkes, L.M., Rashid, W., Chard, D.T., Tofts, P.S., 2004. Normal cerebral perfusion measurements using arterial spin labeling: Reproducibility, stability, and age and gender effects. Magn. Reson. Med. 51 (4), 736–743. http://dx.doi.org/10.1002/mrm.20023.

Paschoal, A.M., Leoni, R.F., Pastorello, B.F., van Osch, M.J.P., 2021. Three-dimensional gradient and spin-echo readout for time-encoded pseudo-continuous arterial spin labeling: Influence of segmentation factor and flow compensation. Magn. Reson. Med. 86 (3), 1454–1462. http://dx.doi.org/10.1002/mrm.28807.

Plenge, E., Poot, D.H.J., Bernsen, M., Kotek, G., Houston, G., Wielopolski, P., van der Weerd, L., Niessen, W.J., Meijering, E., 2012. Super-resolution methods in MRI: Can they improve the trade-off between resolution, signal-to-noise ratio, and acquisition time? Magn. Reson. Med. 68 (6), 1983–1993. http://dx.doi.org/10.1002/mrm.24187.

Poot, D.H.J., Jeurissen, B., Bastiaensen, Y., Veraart, J., Van Hecke, W., Parizel, P.M., Sijbers, J., 2013. Super-resolution for multislice diffusion tensor imaging. Magn. Reson. Med. 69 (1), 103–113. http://dx.doi.org/10.1002/mrm.24233.

Poot, D.H.J., Van Meir, V., Sijbers, J., 2010. General and efficient super-resolution method for multi-slice MRI. In: Medical Image Computing and Computer-Assisted Intervention–MICCAI 2010, Vol. 6361. pp. 615–622. http://dx.doi.org/10.1007/978-3-642-15705-9_75.

Qin, Q., Alsop, D.C., Bolar, D.S., Hernandez-Garcia, L., Meakin, J., Liu, D., Nayak, K.S., Schmid, S., van Osch, M.J.P., Wong, E.C., Woods, J.G., Zaharchuk, G., Zhao, M.Y., Zun, Z., Guo, J., the ISMRMPerfusion Study Group, 2022. Velocity-selective arterial spin labeling perfusion MRI: A review of the state of the art and recommendations for clinical implementation. Magn. Reson. Med. 88 (4), 1528–1547. http://dx.doi.org/10.1002/mrm.29371.

Ramos-Llordén, G., den Dekker, A.J., Van Steenkiste, G., Jeurissen, B., Vanhevel, F., Van Audekerke, J., Verhoye, M., Sijbers, J., 2017. A unified maximum likelihood framework for simultaneous motion and T_1 estimation in quantitative MR T_1 mapping. IEEE Trans. Med. Imaging 36 (2), 433–446. http://dx.doi.org/10.1109/TMI.2016.2611653.

Scheffler, K., 2002. Superresolution in MRI? Magn. Reson. Med. 48 (2), 408. http://dx.doi.org/10.1002/mrm.10203.

Setsompop, K., Bilgic, B., Nummenmaa, A., Fan, Q., Cauley, S.F., Huang, S., Chatnuntawech, I., Rathi, Y., Witzel, T., Wald, L.L., 2015. SLIce Dithered Enhanced Resolution Simultaneous MultiSlice (SLIDER-SMS) for high resolution (700 um) diffusion imaging of the human brain. In: Proc. Intl. Soc. Mag. Reson. Med., Vol. 23. p. 339.

Shao, X., Wang, Y., Moeller, S., Wang, D.J., 2018. A constrained slice-dependent background suppression scheme for simultaneous multislice pseudo-continuous arterial spin labeling. Magn. Reson. Med. 79 (1), 394–400. http://dx.doi.org/10.1002/mrm.26643.

Shilling, R.Z., Robbie, T.Q., Bailloeul, T., Mewes, K., Mersereau, R.M., Brummer, M.E., 2009. A super-resolution framework for 3-D high-resolution and high-contrast imaging using 2-D multislice MRI. IEEE Trans. Med. Imaging 28 (5), 633–644. http://dx.doi.org/10.1109/TMI.2008.2007348.

Shou, Q., Shao, X., Wang, D.J.J., 2021. Super-resolution arterial spin labeling using slice-dithered enhanced resolution and simultaneous multi-slice acquisition. Front. Neurosci. 15, http://dx.doi.org/10.3389/fnins.2021.737525.

Smith, S.M., Jenkinson, M., Woolrich, M.W., Beckmann, C.F., Behrens, T.E., Johansen-Berg, H., Bannister, P.R., De Luca, M., Drobnjak, I., Flitney, D.E., Niazy, R.K., Saunders, J., Vickers, J., Zhang, Y., De Stefano, N., Brady, J.M., Matthews, P.M., 2004. Advances in functional and structural MR image analysis and implementation as FSL. NeuroImage 23, S208–S219. http://dx.doi.org/10.1016/j.neuroimage.2004.07.051.

Teeuwisse, W.M., Schmid, S., Ghariq, E., Veer, I.M., van Osch, M.J., 2014. Time-encoded pseudocontinuous arterial spin labeling: Basic properties and timing strategies for human applications. Magn. Reson. Med. 72 (6), 1712–1722. http://dx.doi.org/10.1002/mrm.25083.

Teeuwisse, W.M., Webb, A.G., van Osch, M.J.P., 2010. Arterial spin labeling at ultra-high field: All that glitters is not gold. Int. J. Imaging Syst. Technol. 20 (1), 62–70. http://dx.doi.org/10.1002/ima.20218.

Van Dyck, P., Smekens, C., Vanhevel, F., De Smet, E., Roelant, E., Sijbers, J., Jeurissen, B., 2020. Super-resolution magnetic resonance imaging of the knee using 2-dimensional turbo spin echo imaging. Invest. Radiol. 55 (8), 481–493. http://dx.doi.org/10.1097/RLI.0000000000000676.

van Osch, M.J.P., Teeuwisse, W.M., Chen, Z., Suzuki, Y., Helle, M., Schmid, S., 2018. Advances in arterial spin labelling MRI methods for measuring perfusion and collateral flow. J. Cereb. Blood. Flow. Metab. 38 (9), 1461–1480. http://dx.doi.org/10.1177/0271678X17713434.

Van Reeth, E., Tham, I.W., Tan, C.H., Poh, C.L., 2012. Super-resolution in magnetic resonance imaging: A review. Concepts Magn. Reson. 40A (6), 306–325. http://dx.doi.org/10.1002/cmr.a.21249.

Van Steenkiste, G., Jeurissen, B., Veraart, J., den Dekker, A.J., Parizel, P.M., Poot, D.H.J., Sijbers, J., 2016. Super-resolution reconstruction of diffusion parameters from diffusion-weighted images with different slice orientations. Magn. Reson. Med. 75 (1), 181–195. http://dx.doi.org/10.1002/mrm.25597.

Van Steenkiste, G., Poot, D.H.J., Jeurissen, B., den Dekker, A.J., Vanhevel, F., Parizel, P.M., Sijbers, J., 2017. Super-resolution T1 estimation: Quantitative high resolution T1 mapping from a set of low resolution T1-weighted images with different slice orientations. Magn. Reson. Med. 77 (5), 1818–1830. http://dx.doi.org/10.1002/mrm.26262.

Vidorreta, M., Balteau, E., Wang, Z., De Vita, E., Pastor, M.A., Thomas, D.L., Detre, J.A., Fernández-Seara, M.A., 2014. Evaluation of segmented 3D acquisition schemes for whole-brain high-resolution arterial spin labeling at 3T. NMR Biomed. 27 (11), 1387–1396. http://dx.doi.org/10.1002/nbm.3201.

Vidorreta, M., Wang, Z., Rodríguez, I., Pastor, M.A., Detre, J.A., Fernández-Seara, M.A., 2013. Comparison of 2D and 3D single-shot ASL perfusion fMRI sequences. NeuroImage 66, 662–671. http://dx.doi.org/10.1016/j.neuroimage.2012.10.087.

Woolrich, M.W., Jbabdi, S., Patenaude, B., Chappell, M.A., Makni, S., Behrens, T., Beckmann, C., Jenkinson, M., Smith, S.M., 2009. Bayesian analysis of neuroimaging data in FSL. NeuroImage 45 (1, Supplement 1), S173–S186. http://dx.doi.org/10.1016/j.neuroimage.2008.10.055.

Ye, F.Q., Frank, J.A., Weinberger, D.R., McLaughlin, A.C., 2000. Noise reduction in 3D perfusion imaging by attenuating the static signal in arterial spin tagging (ASSIST). Magn. Reson. Med. 44 (1), 92–100. http://dx.doi.org/10.1002/1522-2594(200007)44:1<92::AID-MRM14>3.0.CO;2-M.

Zhang, K., Herzog, H., Mauler, J., Filss, C., Okell, T.W., Kops, E.R., Tellmann, L., Fischer, T., Brocke, B., Sturm, W., Coenen, H.H., Shah, N.J., 2014. Comparison of Cerebral Blood Flow Acquired by Simultaneous [^{15}O]Water Positron Emission Tomography and Arterial Spin Labeling Magnetic Resonance Imaging. J. Cereb. Blood Flow Metab. 34 (8), 1373–1380. http://dx.doi.org/10.1038/jcbfm.2014.92.